catalysts

MDPI

Article

Multifunctional EDTA-Stabilized Ni-Oleate/ZnO Hybrid Nano-Additive for Simultaneous Desulfurization, Octane Enhancement, and Vapor Pressure Control in Refinery Gasoline: Characterization and DFT Mechanistic Insights

Ibrahim A. Kareem Al-Dulaimi [1,*], Abbas J. Sultan [2,*], Luma H. Mahmoud [2], Thaer Al-Jadir [3,4], Bashar J. Kadhim [2], Zainab A. Abd Oun [1], Dalal Abbas Fadhil [2], Haydar A. S. Aljaafari [2], Laith S. Sabri [2], Shurooq Talib Al-Humairi [2] and Muthanna H. Al-Dahhan [5]

1 Research and Quality Control Department, Al-Daura Refinery, Midland Refineries Company (MRC), Baghdad 10022, Iraq
2 College of Chemical Engineering, University of Technology-Iraq, Baghdad 10066, Iraq; haydar.al.jaafari@uotechnology.edu.iq (H.A.S.A.)
3 Environment Research Center, University of Technology-Iraq, Baghdad 10066, Iraq
4 Oil and Gas Engineering Department, University of Warith Al-Anbiyaa, Karbala 56001, Iraq
5 Department of Chemical and Biochemical Engineering, Missouri University of Science and Technology, Rolla, MO 65409, USA
* Correspondence: ibra88822@gmail.com (I.A.K.A.-D.); abbas.j.sultan@uotechnology.edu.iq (A.J.S.)

Abstract

A novel EDTA@Ni-oleate/ZnO hybrid liquid additive was synthesized using a three-step coordination chemistry process and evaluated for gasoline upgrading under ambient blending conditions without externally supplied hydrogen. The additive was characterized using ATR-FTIR, UV-Vis spectroscopy, dynamic light scattering (DLS), field-emission scanning electron microscopy (FESEM), and X-ray diffraction (XRD). At the same time, gas chromatography–mass spectrometry (GC-MS) and density functional theory (DFT) calculations were employed to investigate changes in fuel composition and possible sulfur–material interactions. Spectroscopic and structural analyses provided evidence consistent with the formation of a hybrid coordination system containing Ni-oleate and ZnO-related components. DLS measurements of the freshly prepared dispersion in xylene showed an effective hydrodynamic diameter of 30.5 nm and a polydispersity index of 0.005. A laboratory-prepared formulation containing 350 mL of refinery gasoline, 40 mL of toluene, and 8 mL of the hybrid additive exhibited a decrease in measured sulfur concentration from 149.6 to 124.0 ppm, an increase in research octane number (RON) from 77.0 to 83.5, and a decrease in Reid vapor pressure (RVP) from 7.9 to 7.6 psi. A gasoline–toluene reference blend exhibited a RON of 80.4, demonstrating the substantial contribution of toluene to the overall octane enhancement. The observed sulfur concentration decrease includes blending dilution effects, and the contribution of chemical adsorption could not be independently quantified. GC-MS analysis indicated changes in relative hydrocarbon peak-area distributions but did not establish selective hydrocarbon removal. DFT calculations provided molecular-level insights into possible interactions between dibenzothiophene and the investigated Ni-EDTA and ZnO models, although the proposed adsorption mechanism remains experimentally unconfirmed. These findings demonstrate changes in sulfur concentration, RON, and RVP for the investigated laboratory formulation and identify opportunities for further evaluation of its fuel-upgrading performance and practical applicability.

Check for updates

Academic Editor: Diego Luna

Received: 22 October 2026
Revised: 11 November 2026
Accepted: 12 November 2026
Published: 18 November 2026

Copyright: © 2026 by the authors. Licensee MDPI, Basel, Switzerland. This article is an open access article distributed under the terms and conditions of the Creative Commons Attribution (CC BY) license.

Keywords: sulfur reduction; Ni-oleate; ZnO nanoparticles; EDTA chelation; vapor pressure; DFT; gasoline upgrading

1. Introduction

The demand for ultra-low-sulfur transportation fuels has increased significantly over the past two decades, primarily due to increasingly stringent international environmental regulations. The European Union Directive 2009/30/EC sets a maximum sulfur content of 10 ppm in commercial gasoline, aiming to reduce sulfur oxides (SO_x) emissions, which contribute to acid rain and fine particulate matter (PM2.5) [1]. Similarly, China's National VI fuel standards and the International Maritime Organization's IMO 2020 sulfur cap for marine fuels reflect a global trend toward reducing sulfur levels across all hydrocarbon energy sources [2,3]. In addition to atmospheric pollution, sulfur-containing compounds in gasoline can contribute to the poisoning and deactivation of platinum-group metal catalysts in three-way catalytic converters (TWCs), adversely affecting their emission-control performance. This process accelerates catalyst deactivation and increases emissions of unburned hydrocarbons, carbon monoxide, and nitrogen oxides [4,5]. These combined regulatory and technical challenges necessitate the development of effective, scalable desulfurization strategies that overcome the economic limitations of conventional refinery processes.

Conventional hydrodesulfurization (HDS) using sulfided Co-Mo or Ni-Mo catalysts remains the industrial standard for sulfur removal. However, this process exhibits several well-documented limitations, including potential RON losses associated with olefin hydrogenation, hydrogen consumption, and significant capital investment requirements [6–9]. Additionally, refractory compounds such as sterically hindered 4,6-dimethyldibenzothiophene (4,6-DMDBT) are resistant to hydrogenolysis under standard operating conditions [10,11]. These challenges have prompted extensive research into alternative, hydrogen-free desulfurization strategies [12,13].

Alternative desulfurization approaches, including oxidative desulfurization (ODS), extractive desulfurization (EDS), adsorptive desulfurization (ADS), and biodesulfurization, have demonstrated promising performance characteristics in laboratory and pilot-scale studies [14–18]. ODS utilizes oxidants such as hydrogen peroxide or molecular oxygen to convert organosulfur compounds into polar sulfoxides and sulfones, which are then extracted [19]. EDS leverages the differential solubility of sulfur species in ionic liquids, deep eutectic solvents, or polyethylene glycol systems to achieve selective partitioning [20]. ADS uses solid adsorbents such as zeolites, activated carbons, metal oxides, and metal–organic frameworks (MOFs) for sulfur capture under ambient conditions [21–25]. Despite advances in reactive adsorption, extractive, oxidative, and metal-based desulfurization technologies, the simultaneous evaluation of sulfur concentration, research octane number (RON), and Reid vapor pressure (RVP) under ambient gasoline-blending conditions remains an area of interest. This motivates the present investigation of a multifunctional hybrid formulation, while recognizing that the contributions of chemical adsorption, blending dilution, and individual formulation components require careful distinction [12,26,27].

The present EDTA@Ni-oleate/ZnO hybrid formulation was evaluated through ambient-temperature gasoline blending without externally supplied hydrogen. This approach differs from reactive adsorption desulfurization (RADS), which generally employs solid adsorbents under elevated-temperature conditions. Previous research using NiO/ZnO-Al_2O_3-SiO_2 adsorbents demonstrated reactive sulfur removal at 300 °C and investigated hydrogen-assisted adsorbent activation [28]. In contrast, the present formulation achieved a decrease in measured sulfur concentration from 149.6 to 124.0 ppm under ambient blending condi-

tions. However, this decrease includes dilution effects, and the contributions of physical separation and chemical adsorption have not been independently quantified. Therefore, the sulfur-removal efficiency of the present formulation cannot be directly compared with that of established RADS technologies. Another relevant approach involves hydrocarbon-soluble metal carboxylate systems. Oil-soluble zinc carboxylate oxo complexes have been proposed for hydrogen sulfide (H2S) scavenging from hydrocarbon streams [29]. Although these systems share certain chemical characteristics with the present formulation, they differ in their composition and primary sulfur-treatment objectives. In addition to the measured sulfur concentration decrease, the complete gasoline formulation exhibited an increase in research octane number (RON) from 77.0 to 83.5 and a decrease in Reid vapor pressure (RVP) from 7.9 to 7.6 psi. The gasoline–toluene reference blend exhibited a RON of 80.4, confirming that toluene contributed substantially to the overall octane enhancement. The additional 3.1 RON-unit increase associated with the complete hybrid formulation cannot be attributed exclusively to the nanoparticles because the individual contributions of the carrier and additive constituents were not independently determined. Thus, the main distinguishing feature of the present study is the evaluation of a hybrid liquid formulation that combines changes in sulfur concentration, RON, and RVP under ambient laboratory blending conditions. Nevertheless, its comparative desulfurization performance, industrial applicability, and economic competitiveness remain to be established. Further investigations of additive separation, residual metal concentrations, colloidal stability, regeneration, and techno-economic feasibility are required before practical advantages over established desulfurization technologies can be confirmed.

Transition-metal carboxylate nanoparticle systems and EDTA-chelated coordination networks have exhibited significant catalytic and adsorptive properties in hydrocarbon matrices [30–33]. Nickel (II) centers can act as Lewis acid sites and may interact with suitable sulfur-containing molecules through coordination interactions [34,35]. Carboxylate-coordinated nickel compounds, including Ni-oleate, contain organic chains that may improve their compatibility with hydrocarbon media [36,37]. Zinc oxide (ZnO) is also of interest in sulfur-treatment applications because its surface sites can participate in interactions with sulfur-containing species [8,24]. EDTA (ethylenediaminetetraacetic acid) is a multidentate chelating ligand that can influence metal coordination and dispersion behavior [30,31]. In the present study, Ni-oleate, EDTA-stabilized ZnO, and a xylene carrier were combined to prepare a hybrid liquid additive. The resulting formulation was investigated experimentally, while possible interactions with a model organosulfur compound were examined using DFT calculations. However, the proposed coordination and sulfur-interaction mechanisms have not been independently established under actual gasoline-treatment conditions.

Gasoline produced by Iraqi refineries, including output from the Al-Daura Refinery in Baghdad, one of the country's largest and most strategically significant fuel-processing facilities, typically has a baseline research octane number (RON) of 75–80 and sulfur concentrations of 100–200 ppm. This composition reflects a high n-alkane content and limited access to reformate blending stocks [38,39]. These properties position Iraqi gasoline at a disadvantage relative to emerging national and international fuel quality standards, creating a need for cost-effective, drop-in upgrading strategies that do not require significant refinery capital investment. The present study investigates whether an EDTA@Ni-oleate/ZnO-based formulation can improve selected fuel-quality parameters under ambient laboratory blending conditions. However, its suitability for refinery-scale application, including additive separation, residual-metal control, process integration, and economic feasibility, remains to be established [12,38,39].

The objectives of this study are as follows: (i) to synthesize and characterize an EDTA@Ni-oleate/ZnO hybrid liquid additive using a three-step synthesis procedure; (ii) to evaluate changes in sulfur concentration, research octane number (RON), and Reid vapor pressure (RVP) following laboratory blending with Al-Daura refinery gasoline; (iii) to characterize the physicochemical properties of the prepared formulation using FTIR, UV-Vis, DLS, FESEM, and XRD, and to examine changes in relative hydrocarbon-group distributions using GC-MS; and (iv) to investigate possible molecular interactions between dibenzothiophene (DBT) and simplified Ni-EDTA and ZnO models using density functional theory (DFT) calculations. The study provides experimental observations and computational insights into the investigated formulation, while recognizing that the contributions of individual additive components, the proposed sulfur-removal mechanism, and industrial applicability require further verification.

2. Results and Discussion

2.1. Structural Characterization: FTIR Analysis

The ATR-FTIR spectrum of the EDTA@Ni-oleate/ZnO hybrid additive (Figure 1) exhibits characteristic absorption bands associated with aliphatic chains, carboxylate groups, and metal–oxygen interactions. These features are consistent with the presence of the principal components of the proposed hybrid formulation, although the detailed molecular coordination structure cannot be established from FTIR analysis alone.

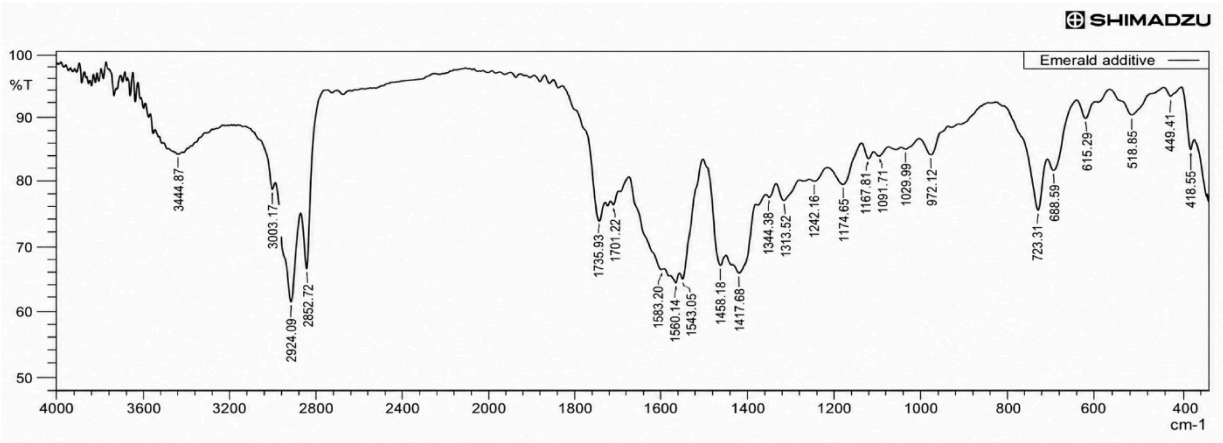


Figure 1. ATR-FTIR spectrum of the EDTA@Ni-oleate/ZnO hybrid additive, recorded using a Shimadzu IRTracer-100 spectrometer in the range of 400–4000 cm^{-1} with a resolution of 4 cm^{-1}.

Strong methylene stretching bands at 2924.09 cm^{-1} (asymmetric CH_2 stretching) and 2852.72 cm^{-1} (symmetric CH_2 stretching) are consistent with the long aliphatic chains of the oleate-containing formulation. The weak absorption at 3003.17 cm^{-1} is consistent with olefinic =C-H stretching and suggests the presence of unsaturated hydrocarbon chains. The CH_2 rocking mode at 723.31 cm^{-1} further supports the presence of a long, uninterrupted methylene sequence, consistent with an extended C18 alkyl chain [36,37].

The carboxylate stretching region (1380–1650 cm^{-1}) provides evidence consistent with metal–carboxylate interactions. Absorption bands at 1593.20 and 1560.41 cm^{-1} are assigned to asymmetric COO− stretching vibrations, while bands at 1458.18 and 1417.68 cm^{-1} are associated with symmetric COO− stretching vibrations. The separation between the bands at 1593.20 and 1458.18 cm^{-1} is approximately 135 cm^{-1}, which may be consistent with a coordinated carboxylate environment. However, the coordination mode cannot be determined unambiguously from this separation alone because multiple carboxylate environments and overlapping vibrational bands may be present. Weak absorptions

at 1735.93 and 1701.22 cm^{-1} may indicate residual protonated carboxylic acid groups or other carbonyl-containing species. Therefore, these spectral features support the presence of carboxylate-containing components but do not establish complete ligand substitution or a unique coordination geometry [36,37].

Absorption bands at 1344.38 and 1313.52 cm^{-1} may include contributions from C– N stretching vibrations associated with EDTA-containing species [40,41]. However, these bands alone do not independently confirm the coordination of EDTA nitrogen atoms to nickel centers. The broad absorption at 3444.87 cm^{-1} may arise from O-H stretching associated with residual moisture, hydroxyl-containing species, or hydrogen-bonded carboxylic acid groups. The shoulder at 1543.05 cm^{-1} may involve overlapping vibrations from carboxylate-containing species, although its specific assignment remains uncertain. Collectively, these spectral features are compatible with the proposed formulation but do not uniquely establish the detailed EDTA coordination environment.

Absorption bands at 518.85 and 449.41 cm^{-1} are consistent with metal–oxygen vibrational contributions that may be associated with ZnO-containing components [42,43]. The band at 615.29 cm^{-1} may involve Ni-O or other metal–oxygen vibrations, while the feature at 418.55 cm^{-1} lies within a region where inorganic lattice vibrations may occur. However, these assignments are not unique, and FTIR analysis alone cannot confirm the crystalline phases or detailed arrangement of the inorganic components. An additional absorption at 972.12 cm^{-1} may involve an out-of-plane olefinic C-H deformation, but this band does not independently confirm retention of the original cis configuration of the oleate double bond.

Overall, the ATR-FTIR spectrum exhibits features consistent with long-chain organic groups, carboxylate-containing species, and possible metal–oxygen interactions within the prepared formulation. The carboxylate stretching bands suggest interactions involving metal centers, while the lower-wavenumber absorptions are compatible with contributions from inorganic components. These observations support the proposed hybrid formulation but do not independently establish a unique molecular coordination geometry, complete ligand substitution, or a core–shell nanostructure. Additional morphological and structural information is discussed in Sections 2.5 and 2.6 using FESEM and XRD, respectively.

2.2. Electronic Structure Characterization Using UV-Vis Spectroscopy

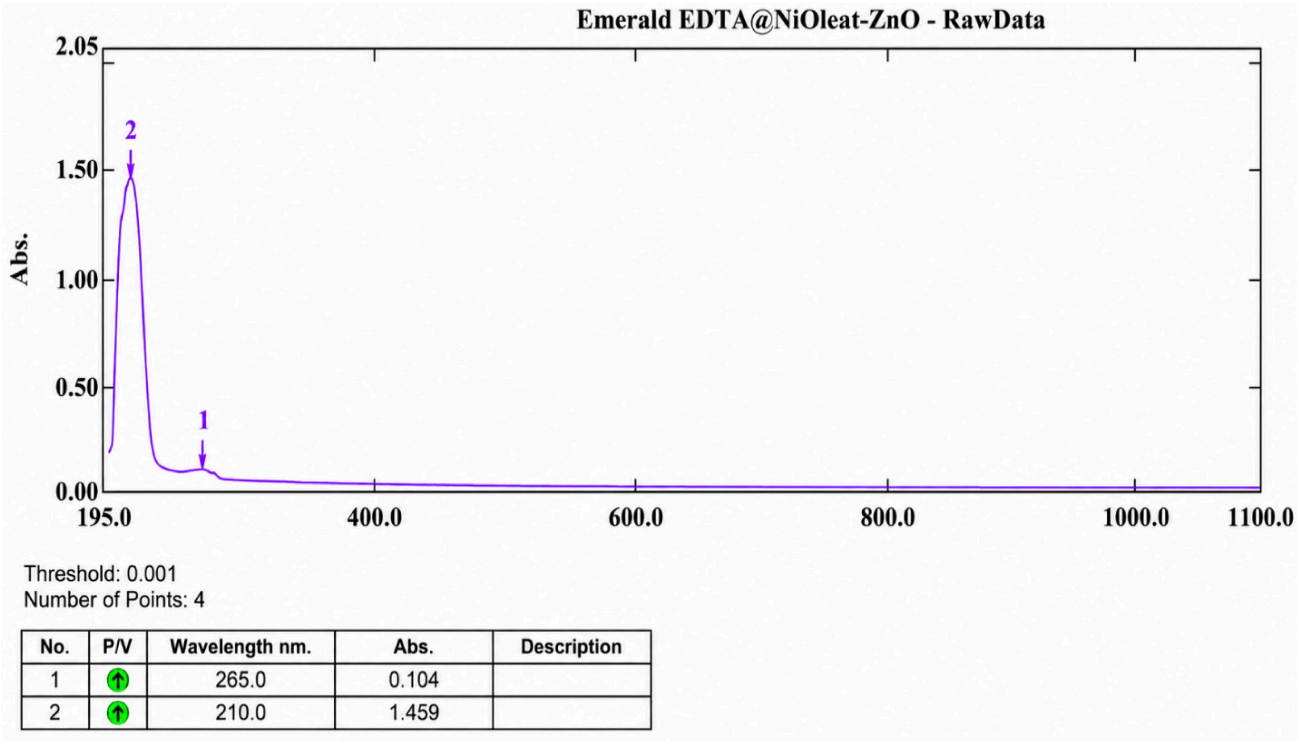
The UV-Vis absorption spectrum of the EDTA@Ni-oleate/ZnO hybrid additive, measured in analytical-grade xylene from 195 to 1100 nm, exhibits two distinct absorption features in the near-UV region and no detectable absorption above 400 nm, as illustrated in Figure 2.

An intense absorption feature was recorded near 210 nm (absorbance = 1.459). Absorption in this region may involve electronic transitions associated with organic components of the formulation. However, the oleate double bond is not directly conjugated with the carboxylate group, and the observed feature cannot be uniquely assigned to a conjugated $C{=}C\text{-}COO^{-}$ system. The reliability and molecular origin of this absorption require consideration of the solvent background and instrumental measurement conditions [36,44].

A weaker absorption feature was recorded near 265 nm (absorbance = 0.104). Although charge-transfer transitions may occur in metal–ligand coordination systems, the available spectrum does not establish that this feature originates specifically from ligand-to-metal charge transfer involving Ni^{2+}. Other organic electronic transitions and contributions from the solvent background cannot be excluded. Therefore, the assignment of this band remains tentative [44].

The difference in recorded absorbance between the features at 210 and 265 nm does not independently establish their transition types or relative molar absorptivities [40,44]. In addition, the carboxylate stretching-band separation of approximately 135 cm^{-1} observed

by FTIR (Section 2.1) is consistent with possible metal–carboxylate interactions but does not uniquely establish bidentate coordination [36,40]. Accordingly, the combined spectroscopic observations should be regarded as supporting information rather than definitive evidence of a particular molecular coordination geometry.



No.	P/V	Wavelength nm.	Abs.	Description
1	↑	265.0	0.104	
2	↑	210.0	1.459	

Figure 2. Ultraviolet–visible (UV-Vis) absorption spectrum of the EDTA@Ni-oleate/ZnO hybrid additive in analytical-grade xylene, measured from 195 to 1100 nm. The inset peak table was generated automatically by the instrument software; the green arrows in the P/V column indicate detected peaks (P/V = peak/valley).

No distinct absorption bands were observed in the 400–1100 nm region of the recorded UV–Vis spectrum (Figure 2). However, the absence of resolved visible-region bands does not establish that all nickel centers are incorporated into the proposed coordination framework or exclude the presence of uncoordinated nickel-containing species. Such conclusions would require additional chemical-speciation measurements or appropriate reference spectra.

The UV-Vis observations alone do not establish the availability of Lewis-acid-active Ni2+ sites or demonstrate selective interactions with organosulfur compounds in gasoline. Possible interactions between dibenzothiophene and simplified Ni-EDTA and ZnO models are investigated computationally in Section 2.8. However, the proposed sulfur-adsorption mechanism remains to be verified experimentally.

2.3. Fuel Performance Results

2.3.1. Sulfur Reduction and Proposed Desulfurization Mechanism

The initial sulfur content of commercial unleaded gasoline obtained from the Al-Daura Refinery was measured at 149.6 ppm using ASTM D5453 [45]. Following preparation and centrifugation of the laboratory-scale formulation containing 350 mL of gasoline, 40 mL of toluene, and 8 mL of the EDTA@Ni-oleate/ZnO hybrid additive, the measured sulfur concentration was 124.0 ppm, corresponding to a 17.1% decrease relative to the baseline gasoline.

To assess the possible contribution of blending dilution to the observed decrease in sulfur concentration, an approximate dilution-only concentration was calculated from the nominal blending volumes, assuming that the added components contained no sulfur and that no sulfur removal occurred. This volume-based estimate was 131.6 ppm, whereas the experimentally measured sulfur concentration of the treated blend was 124.0 ± 1.8 ppm (mean ± SD, n = 3), as determined using ASTM D5453 [45]. The numerical difference of 7.6 ppm may reflect effects not represented by the simplified dilution calculation, including differences in component densities, possible sulfur contributions from the added materials, sample separation, and analytical variability, as illustrated in Figure 3. Because a rigorous mass-based sulfur balance and appropriate control measurements were not available, this difference does not independently establish chemical adsorption or quantify sulfur removal by the hybrid additive.

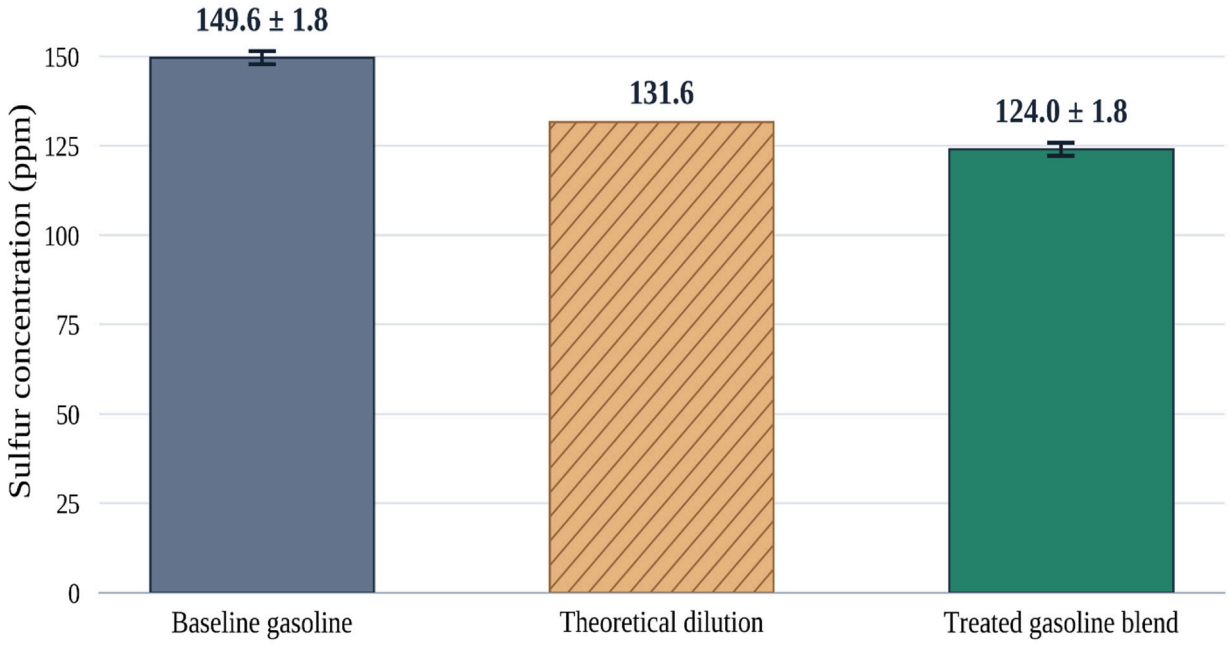


Figure 3. Comparison of sulfur concentrations in baseline gasoline (149.6 ppm), the theoretical dilution estimate (131.6 ppm), and the EDTA@Ni-oleate/ZnO-treated gasoline blend (124.0 ppm). Error bars represent ±1 standard deviation (SD) from triplicate measurements (n = 3) for the experimentally measured values. The theoretical dilution estimate was calculated from the blending proportions.

These results demonstrate a decrease in the measured sulfur concentration of the laboratory-prepared gasoline blend under ambient blending conditions without externally supplied hydrogen. However, the individual contributions of dilution, physical separation, and possible sulfur adsorption cannot be conclusively determined from the available measurements. Coordination interactions between organosulfur compounds and metal-containing sites in the hybrid formulation remain a proposed mechanism rather than an experimentally confirmed explanation. The DFT calculations discussed in Section 2.8 provide theoretical insights into possible interactions involving dibenzothiophene but do not independently verify chemical sulfur removal under the investigated gasoline-treatment conditions.

The proposed sulfur-interaction mechanism may involve coordination between suitable organosulfur compounds and metal-containing sites in the hybrid formulation. However, the available GC-MS data do not independently establish selective adsorption or identify the sulfur-containing compounds responsible for the measured concentration decrease. Unlike conventional hydrodesulfurization (HDS), which generally requires elevated temperatures,

hydrogen pressure, and specialized processing equipment, the present fuel formulation was evaluated under ambient laboratory blending conditions without externally supplied hydrogen during treatment [46,47]. Nevertheless, the present results do not establish comparable sulfur-removal performance, industrial feasibility, or an economic advantage over established HDS technologies.

2.3.2. Fuel Performance of the Investigated Refinery Gasoline Blend

Table 1 summarizes the measured fuel properties of the baseline gasoline and the investigated gasoline blends, including the formulation containing the EDTA@Ni-oleate/ZnO hybrid additive and toluene. The three key performance indicators—sulfur concentration, research octane number (RON), and Reid vapor pressure (RVP)—were evaluated for the complete formulation. The results show simultaneous changes in these properties under ambient laboratory blending conditions. However, these changes reflect the behavior of the complete formulation and cannot be attributed exclusively to the hybrid additive because the contributions of the individual blending components were not independently quantified.

Table 1. Comparison of sulfur concentration, research octane number (RON), and Reid vapor pressure (RVP) for baseline gasoline and the investigated blends.

Property	Baseline Gasoline	Small-Scale Treatment	Gasoline + Additive	Gasoline + Toluene (Without Additive)	Gasoline + Additive + Toluene
Sulfur (ppm)	149.6 ± 1.8	~123–130	122.8	NR	124.0 ± 1.8
RON	77.0 ± 0.2	NR	79.7	80.4	83.5 ± 0.2
RVP (psi)	7.9 ± 0.05	~11.0	11.0	NR	7.6 ± 0.05
Sulfur Reduction (%)	—	~13.1–17.8%	17.9%	NR	17.1%
RON gain (units) [b]	—	NR	+2.7	+3.4	+6.5

Notes: NR = not reported; — = not applicable; [b] Preliminary Scherrer crystallite-size estimates for tentatively assigned inorganic phases.

Sulfur content decreased from 149.6 ppm in the baseline gasoline to 124.0 ppm in the treated blend, corresponding to a 17.1% decrease in measured concentration, as discussed in Section 2.3.1. The gasoline–toluene reference blend contained approximately 10.26 vol% toluene, whereas the complete formulation contained approximately 10.05 vol% toluene and 2.01 vol% hybrid additive, based on the nominal volumes of the blending components. The RON increased from 77.0 to 83.5, representing an overall gain of 6.5 units. The gasoline–toluene reference blend, prepared without the hybrid additive, had a RON of 80.4, corresponding to a gain of 3.4 units over the baseline gasoline. Thus, toluene contributed substantially to the observed octane enhancement. The complete formulation had RON 3.1 units higher than the toluene-only reference blend. This difference represents the effect associated with adding the complete hybrid formulation under the tested conditions; it does not isolate the contribution of the nanoparticles from that of the carrier and other additive constituents.

The present study evaluated the fuel performance of the complete EDTA@Ni-oleate/ZnO hybrid additive. However, independent experiments using EDTA@ZnO and Ni-oleate reference formulations at equivalent loadings were not performed. Consequently, the individual contributions of these components to sulfur reduction, RON enhancement, and RVP variation cannot be determined from the present results. Furthermore, the available experimental results are insufficient to determine whether combining these components produces a synergistic effect. Future studies should compare EDTA@ZnO, Ni-oleate, and

the complete hybrid additive under identical blending and analytical conditions, including appropriate solvent and carrier controls, to quantify their individual and combined effects on gasoline properties.

Reid vapor pressure decreased from 7.9 psi in the baseline gasoline to 7.6 psi in the complete formulation, representing a decrease of 0.3 psi (3.8%), as measured according to ASTM D323 [48]. The measured RVP values were below 9.0 psi; however, compliance with a specific regulatory requirement depends on the applicable fuel standard and jurisdiction. The observed RVP decrease may reflect the combined volatility characteristics of gasoline, toluene, and the additive constituents. Because RVP was not measured for the gasoline–toluene reference blend, the independent contribution of the hybrid additive to the observed RVP change cannot be determined. Furthermore, the available GC-MS data do not demonstrate selective removal of volatile hydrocarbons or quantify their contribution to the measured RVP change.

The investigated formulation produced simultaneous changes in the measured sulfur concentration, RON, and RVP under ambient laboratory blending conditions without externally supplied hydrogen. However, these observations do not establish that the hybrid additive selectively removes sulfur-containing compounds or preserves the olefinic fraction. The GC-MS results indicate changes in relative peak-area distributions but do not provide quantitative evidence of complete olefin preservation or selective hydrocarbon removal [46,47]. Furthermore, the gasoline–toluene reference experiment demonstrated that toluene contributed substantially to the overall RON improvement. Therefore, the present results demonstrate the initial performance of the complete fuel formulation, while the individual contributions of the additive constituents and the practical suitability of the treatment require further investigation.

Reported uncertainties (±) represent one standard deviation (SD) from triplicate analytical measurements (n = 3) for the baseline gasoline and the complete gasoline–toluene additive blend. Standard deviations were not reported for the other formulations.

[a] Percentage decrease in measured sulfur concentration relative to baseline gasoline, calculated as $100(C_o - C)/C_o$, where C_o = 149.6 ppm and C is the sulfur concentration of the corresponding sample or blend. These percentages may include blending dilution effects and do not represent independently verified sulfur removal by adsorption.

[b] RON gain relative to baseline gasoline (RON = 77.0).

The gasoline–toluene control contained 350 mL of gasoline and 40 mL of toluene, without the hybrid additive. The complete blend contained 350 mL of gasoline, 40 mL of toluene, and 8 mL of the EDTA@Ni-oleate/ZnO hybrid additive.

The results presented in Table 1 summarize the measured fuel properties of the investigated formulations under ambient blending conditions. The complete formulation decreased the measured sulfur concentration from 149.6 to 124.0 ppm (17.1%), increased RON from 77.0 to 83.5 (+6.5 units), and reduced RVP from 7.9 to 7.6 psi (3.8%), maintaining the RVP below the specified limit of 9.0 psi. The gasoline–toluene reference blend exhibited a RON of 80.4, indicating that toluene contributed substantially to the overall octane enhancement. The additional 3.1 RON-unit increase associated with the complete formulation cannot be attributed exclusively to the nanoparticles because the individual contributions of the carrier and additive constituents were not independently determined. Furthermore, the observed sulfur concentration decrease includes blending dilution, while the GC-MS results do not establish selective removal of n-alkanes or other hydrocarbon classes. Therefore, the results demonstrate the laboratory-scale performance of the complete formulation, although its underlying mechanisms and industrial applicability require further investigation.

2.4. Colloidal Particle Size Characterization via DLS

Dynamic light scattering (DLS) measurements were performed on the EDTA@Ni-oleate/ZnO hybrid additive dispersed in analytical-grade xylene using a Brookhaven Instruments 90Plus analyzer (659 nm, 15° scattering angle, 25.0 ± 0.1 °C). Three independent measurements yielded effective hydrodynamic diameters of 32.9, 29.7, and 28.3 nm. The instrument-reported effective diameter was 30.5 nm, with a calculated mean of 30.3 ± 1.3 nm (mean ± standard error).

The instrument-reported polydispersity index (PDI) was 0.005, indicating a narrow apparent particle-size distribution under the investigated measurement conditions [49].

The low instrument-reported PDI suggests a relatively narrow apparent particle-size distribution for the freshly prepared dispersion in xylene, consistent with the interpretation of DLS measurements described in ISO 22412:2017 [50]. This observation is consistent with initial dispersion of the hybrid formulation, although the individual contributions of EDTA and oleate to dispersion behavior were not independently evaluated. Furthermore, the reported PDI alone does not establish long-term colloidal stability or demonstrate that the formulation is among the most size-uniform systems reported for fuel applications. The particle-size distribution presented in Figure 4 provides a graphical representation of the DLS results under the investigated conditions.

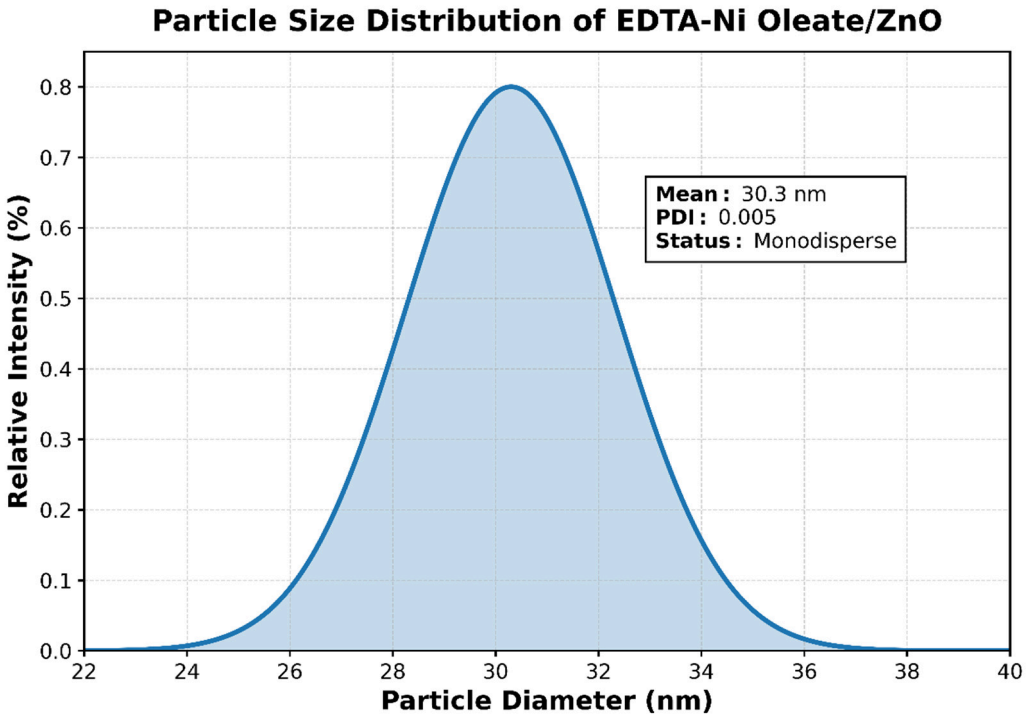


Figure 4. Gaussian particle size distribution of the EDTA@Ni-oleate/ZnO hybrid additive obtained from dynamic light scattering (DLS) measurements (Brookhaven 90Plus, 659 nm, 15°, 25 °C; PDI = 0.005).

The instrument-reported effective hydrodynamic diameter of 30.5 nm may be compared qualitatively with the nanoscale morphological features observed by FESEM (Section 2.5) and the tentative crystallite-size estimates obtained from XRD analysis (Section 2.6). However, these techniques characterize different physical properties. DLS measures hydrodynamic size in dispersion, FESEM provides morphological information from the prepared sample, and XRD estimates coherent crystalline-domain sizes. Therefore, differences among these measurements cannot be used alone to determine the thickness of an organic coordination shell or establish a specific core–shell architecture. Additional struc-

tural characterization would be required to verify the proposed arrangement of inorganic and organic components.

Although the DLS measurements indicated a narrow particle-size distribution for the freshly prepared EDTA@Ni-oleate/ZnO hybrid additive in analytical-grade xylene, these results do not establish its long-term colloidal stability in real gasoline. The effects of extended storage, temperature fluctuations, and water contamination on particle aggregation, sedimentation, and phase separation were not systematically investigated. Therefore, the stability of the hybrid additive under practical fuel storage and handling conditions remains uncertain. Future investigations should evaluate the evolution of particle-size distribution, aggregation behavior, and sedimentation under representative storage temperatures, thermal cycling conditions, and controlled water contamination. Such investigations are essential before considering the formulation for industrial fuel applications.

2.5. Nanoscale Morphology: Field-Emission Scanning Electron Microscopy

Field-emission scanning electron microscopy (FESEM) characterization of the EDTA@Ni-oleate/ZnO hybrid additive was conducted using a TESCAN MIRA3 LMU Schottky field-emission SEM at an accelerating voltage of 15 kV, with secondary electron (SE) detection and a working distance of approximately 10.7 mm. Thirteen images were collected from two spatially independent sample locations (Location 1: StageX = 149.5 µm; Location 2: StageX = 764.7 µm) across a magnification range of 54× to 100,000×, enabling a comprehensive multi-scale morphological analysis from the millimeter to the nanometer scale [51]. The low-magnification FESEM image obtained at 54× is presented in Figure 5.

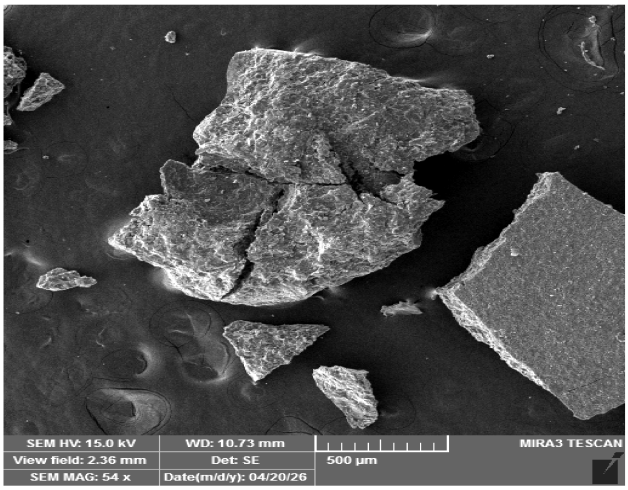
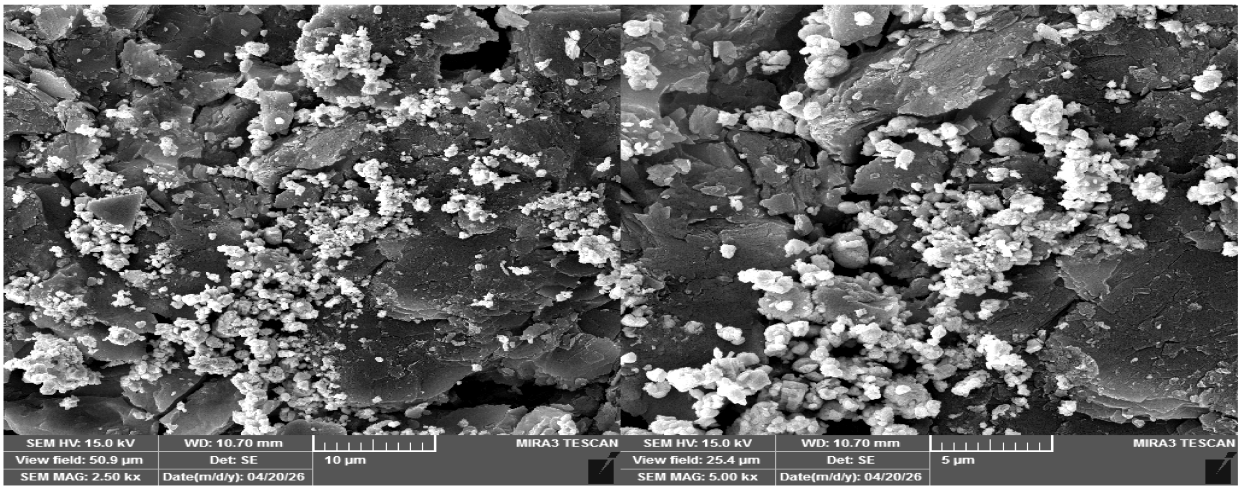


Figure 5. Field emission scanning electron microscopy (FESEM) image of the EDTA@Ni-oleate/ZnO hybrid additive, obtained with a TESCAN MIRA3 LMU at 15 kV using a secondary electron detector, 54× magnification, and a 2.36 mm field of view.

At the lowest magnification (54×, FOV = 2.36 mm, Figure 5), the sample appears as large, flat, platelet-like fragments with rough, textured surfaces. These features suggest the presence of aggregated or layered morphological domains. The low-angle XRD features discussed in Section 2.6 may indicate structural ordering within the material; however, the available FESEM and XRD results do not independently establish a specific smectic-like lamellar coordination network. Furthermore, the observed morphology within the investigated field of view does not establish macroscopic homogeneity of the entire sample.

At low magnifications (2500×–5000×, Figure 6), regions with different morphological features and secondary-electron contrast are observed. Relatively bright, approximately spheroidal aggregates are distributed within darker surrounding regions. These contrast

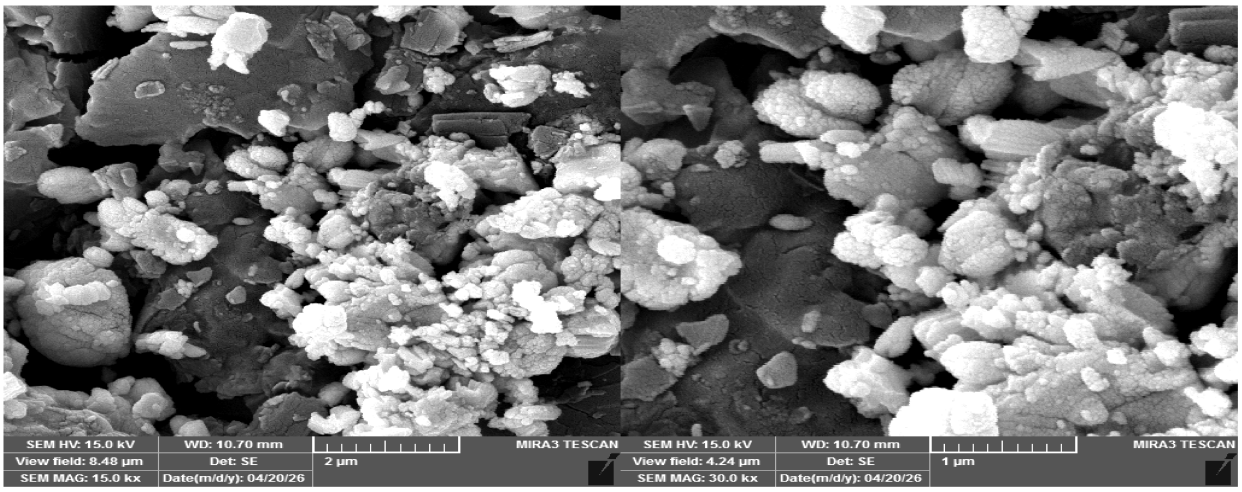
differences may arise from variations in surface topography, local morphology, and imaging conditions. Although the observed features are compatible with a heterogeneous hybrid material, the chemical identities of the bright and dark regions cannot be established from secondary-electron images alone. Elemental mapping or other composition-sensitive characterization would be required to distinguish inorganic and organic components reliably.



(**a**) (**b**)

Figure 6. Field emission scanning electron microscopy (FESEM) low-magnification images acquired at Location 1: (**a**) 2500× magnification (field of view [FOV] = 50.9 µm); (**b**) 5000× magnification (FOV = 25.4 µm).

At medium magnifications (15,000×–30,000×, Figure 7), aggregated nanoscale features with apparent dimensions of approximately 50–200 nm are observed within the surrounding material. Differences in surface morphology and image contrast become more apparent at these magnifications, although the chemical composition of the individual regions remains unconfirmed.

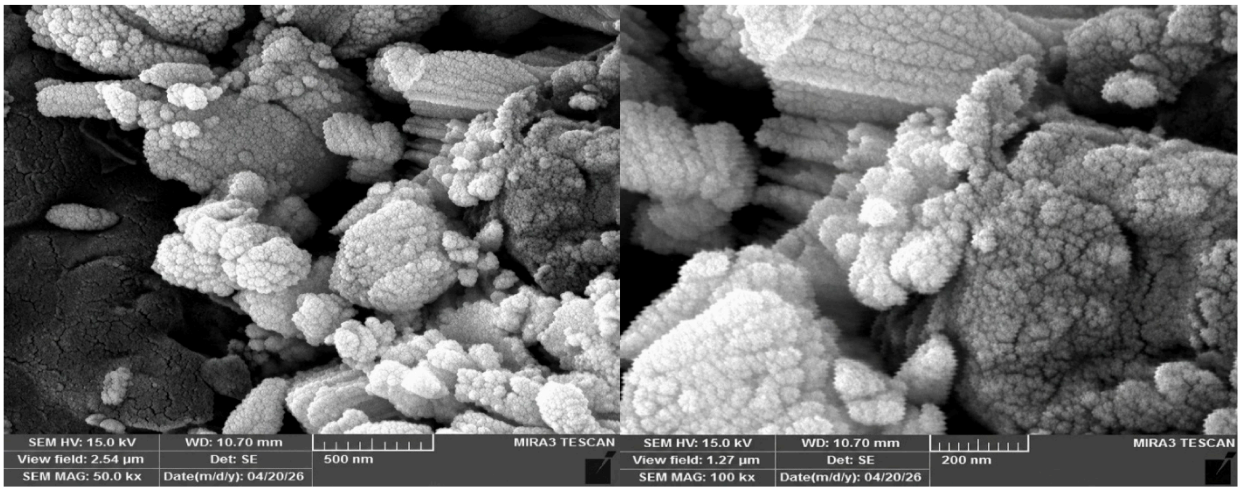


(**a**) (**b**)

Figure 7. FESEM medium-magnification images at Location 1: (**a**) 15,000× (FOV = 8.48 µm); (**b**) 30,000× (FOV = 4.24 µm).

At high magnifications (50,000×–100,000×, Figure 8), fine nanoscale features and aggregates are visible within the prepared material. At 50,000× (Figure 8a), regions containing small, approximately spheroidal features can be distinguished from the surrounding mate-

rial. At 100,000× (Figure 8b; FOV = 1.27 µm; pixel size = 2.484 nm), features with apparent dimensions on the order of 10–20 nm may be present, although their boundaries and dimensions cannot be determined precisely from the available images. The lower-contrast regions surrounding these features cannot be assigned uniquely to an EDTA/oleate organic shell. Consequently, the FESEM observations do not independently establish an organic-shell thickness or quantitatively explain the DLS effective hydrodynamic diameter of 30.5 nm. Additional high-resolution structural and composition-sensitive analyses would be required to confirm the proposed core–shell arrangement [36,49,50].



(**a**) (**b**)

Figure 8. FESEM high-magnification images at Location 1: (**a**) 50,000× (FOV = 2.54 µm); (**b**) 100,000× (FOV = 1.27 µm, pixel size = 2.484 nm).

Additional FESEM images were acquired at a second spatially independent location (Location 2: StageX = 764.7 µm) at magnifications of 15,000×, 30,000×, and 50,000× (Figure 9). The images show morphological features broadly similar to those observed at Location 1, including aggregated structures and regions of differing surface contrast. These observations suggest that similar morphological characteristics occur at both investigated locations. However, examination of two locations alone is insufficient to establish the homogeneity or morphological representativeness of the entire material batch.

In summary, multiscale FESEM characterization reveals morphological features ranging from large platelet-like fragments to smaller aggregates and fine nanoscale structures. The images indicate that the prepared material contains regions with different surface morphologies and contrast characteristics. These observations are compatible with the proposed heterogeneous hybrid formulation but do not independently confirm the chemical composition of individual features, a specific core–shell architecture, or the presence of distinct NiO and ZnO nanocrystallites. Furthermore, FESEM observations cannot establish colloidal stability in gasoline or the availability of Lewis-acid-active sites for organosulfur adsorption. Additional structural and composition-sensitive characterization would be necessary to verify these aspects of the proposed hybrid material [36,51].

Weak diffraction features are observed in the low-angle region, while the experimental pattern exhibits overlapping intensity variations and a broad background at intermediate angles. The features listed in Table 2 at approximately 8.62°, 10.59°, 11.57°, and 12.72° may be associated with structural ordering within the organic Ni-oleate/EDTA matrix. Similarly, the features near 20.23° and 27.48° may reflect contributions from organic-chain packing or other partially ordered components. However, these assignments remain tentative because the available XRD pattern does not provide sufficient resolution to establish a specific

lamellar structure, bilayer repeat arrangement, or crystalline packing form. Additional structural characterization would be required to confirm these interpretations.

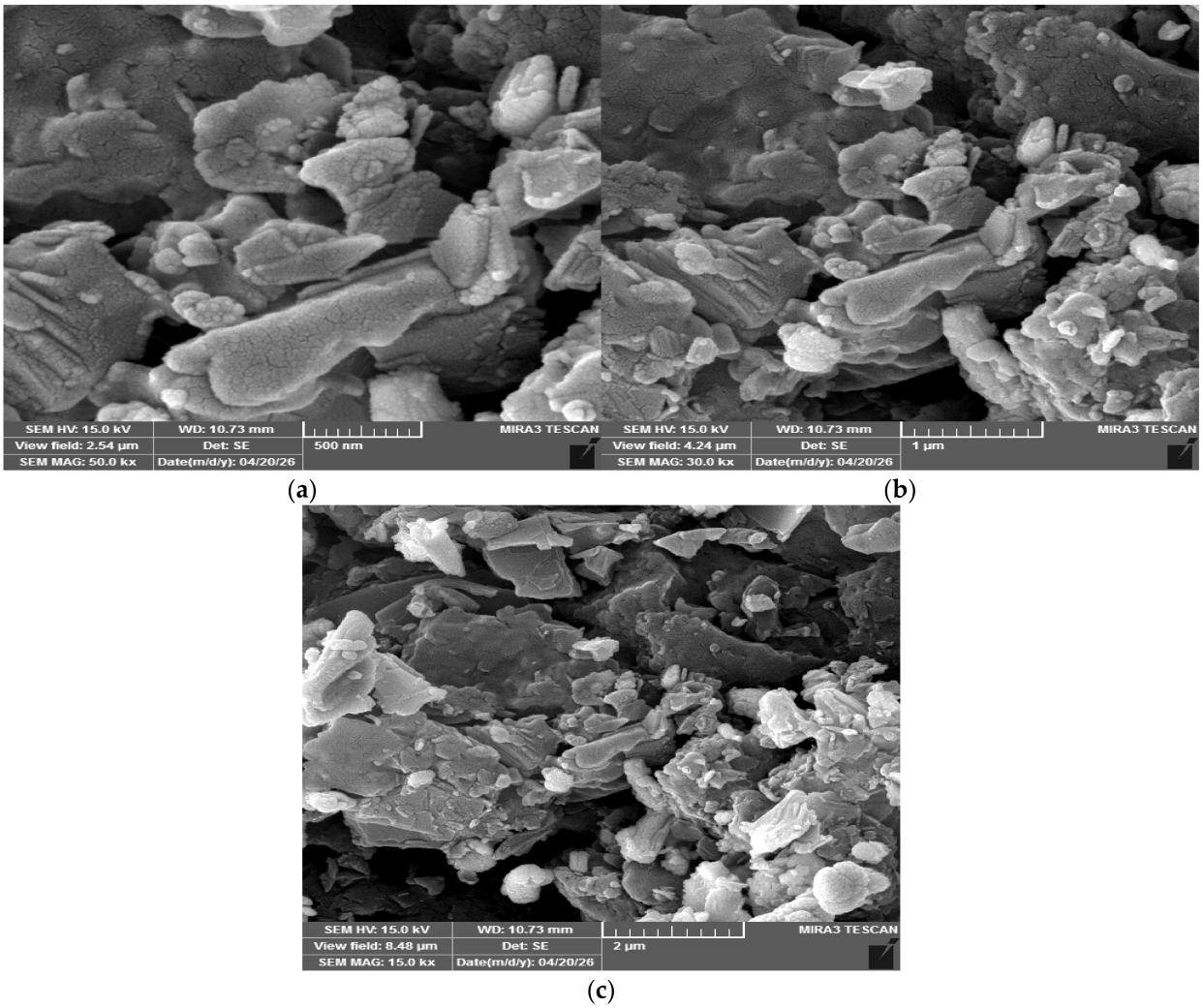


Figure 9. FESEM images at Location 2 (StageX = 764.7 µm) showing morphological features at a second sample location: (**a**) 50,000×; (**b**) 30,000×; (**c**) 15,000×.

2.6. Crystallographic Phase Analysis via X-Ray Diffraction

The powder X-ray diffraction (XRD) pattern of the EDTA@Ni-oleate/ZnO hybrid additive is presented in Figure 10, together with reference diffraction positions for cubic NiO (PDF 47-1049) and hexagonal wurtzite ZnO (PDF 36-1451). The experimental pattern exhibits a broad diffraction background with several overlapping intensity features across the investigated 2θ range of 4.9–80.1°. Comparison with the reference patterns suggests the possible presence of NiO and ZnO crystalline phases within the hybrid material. However, because several reflections are weak or poorly resolved, these phase assignments remain tentative. The low-angle diffraction features may also indicate structural ordering within the organic Ni-oleate/EDTA matrix, although their exact origin cannot be confirmed from the available diffraction data (Table 2) [52,53].

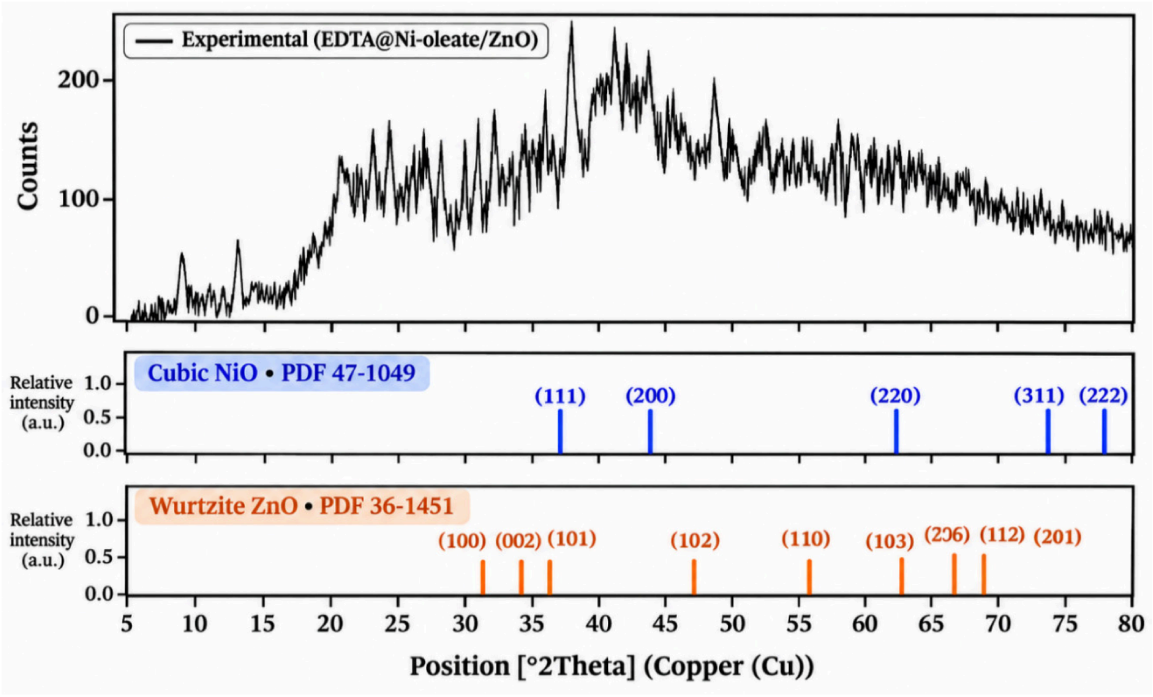


Figure 10. Experimental XRD pattern of the EDTA@Ni-oleate/ZnO hybrid additive compared with reference peak positions for cubic NiO (PDF 47-1049) and wurtzite ZnO (PDF 36-1451). Reference stick heights are schematic, and phase assignments are tentative.

Table 2. Reported XRD features and tentative structural assignments for the EDTA@Ni-oleate/ZnO hybrid additive using Cu Kα radiation (λ = 1.5406 Å).

2θ (°)	d (Å)	FWHM (°)	RI (%)	D (nm)	Tentative Assignment
8.62	10.260	0.394	42.3	—	Possible organic-matrix ordering
10.59	8.352	0.590	13.3	—	Possible organic-matrix ordering
11.57	7.648	0.295	14.1	—	Unassigned low-angle feature
12.72	6.957	0.394	43.1	—	Possible organic-matrix ordering
20.23	4.389	0.590	64.8	—	Possible organic-chain packing
27.48	3.245	0.394	67.6	—	Unassigned intermediate-angle feature
31.60	2.832	0.394	50.4	21.0 *	Possible ZnO (100)
37.36	2.407	0.492	100.0	17.0 *	Possible NiO (111)
43.50	2.081	0.787	58.6	10.9 *	Possible NiO (200)
48.66	1.870	0.720	49.7	—	Unassigned; previously attributed to ZnO (102)

FWHM = full width at half maximum; RI = reported relative intensity; D = reported Scherrer crystallite-size estimate; — = not assigned. * Preliminary Scherrer crystallite-size estimates for tentatively assigned inorganic phases. The reported diffraction parameters are based on the original XRD analysis. Phase assignments and Scherrer crystallite-size estimates are tentative because of overlapping diffraction features and the absence of raw data for independent verification. Crystallite sizes are reported only for potentially identified inorganic phases. The reflection at 48.66° remains unassigned because its correspondence to ZnO (102) could not be confirmed.

The experimental XRD pattern exhibits a broad intensity distribution in the high-angle region, with several overlapping features. Comparison with the reference diffraction positions for cubic NiO (PDF 47-1049) and hexagonal wurtzite ZnO (PDF 36-1451), shown in Figure 10, indicates that these phases may contribute to the observed diffraction profile.

Features reported near 37.36° and 43.50° are close to the principal reference positions of NiO, while the feature near 31.60° is close to a characteristic ZnO reflection. However, the broad background and overlapping signals limit the reliability of individual peak assignments. In particular, the feature reported at 48.66° does not closely match the standard ZnO (102) reflection near 47.5° and therefore requires further verification. Although the original peak-width analysis yielded preliminary crystallite-size estimates of 17.0 nm for the possible NiO phase and 21.0 nm for the possible ZnO phase, these values depend on the reliability of the peak assignments, profile fitting, and instrumental broadening correction. Because the original diffraction data and peak-fitting records are unavailable for independent verification, these values should be regarded as preliminary estimates rather than confirmed crystallite sizes. Additional high-resolution XRD measurements and quantitative phase analysis would be necessary to establish the crystalline phases and their sizes more reliably.

2.7. Molecular Speciation via GC-MS Analysis Before and After Additive Application

Gas chromatography–mass spectrometry (GC-MS) analyses were conducted on baseline Al-Daura gasoline (Sample AH1) and the EDTA@Ni-oleate/ZnO-treated blend (Sample AH2) at the Central Laboratory, University of Kashan, Iran, using an Agilent GC-MS system with acquisition method QC5.M. Mass-spectral library searches were performed using the NIST08 and W10N14 databases to obtain tentative compound assignments. The resulting chromatographic data were used to compare the relative peak-area distributions of hydrocarbon groups before and after treatment. However, these semi-quantitative results do not independently establish chemical desulfurization, selective hydrocarbon removal, or the molecular mechanism responsible for RON enhancement [47,54].

Baseline gasoline composition (Sample AH1). The total ion chromatogram (TIC) of baseline Al-Daura gasoline (Figure 11) reveals 39 distinct peaks within a retention time range of 6.25 to 61.15 min, corresponding to C_5 to C_{19} hydrocarbons. The major hydrocarbon classes are C_4-aromatics (tetramethylbenzenes and ethyldimethylbenzenes, 31.94%), isoalkanes in the C_8 to C_{11} range (26.29%), and C_3-aromatics (trimethylbenzenes and ethylmethylbenzenes, 24.00%), resulting in a total aromatic content of 61.95% (Table 3). The most abundant individual components, 1,2,4-trimethylbenzene (RT = 16.51 min, 7.16% area, library match quality = 97) and 4-ethyl-1,2-dimethylbenzene (RT = 19.52 min, 7.03% area, quality = 95), are high-octane aromatic species that contribute substantially to the fuel's octane rating [47,54].

Figure 11 also shows additional chromatographic signals in the retention-time intervals of approximately 12.0–14.5 min and 27.6–35.3 min. The integration status of these signals cannot be independently established from the available chromatographic records. Although some of these signals may correspond to hydrocarbon isomers, their chemical identities cannot be confirmed from retention times alone. Therefore, no specific compound assignments are made for these unresolved features. According to the original GC-MS library-search report, the peaks at RT = 26.125 and 35.344 min were tentatively assigned to dodecane and tetradecane, respectively. However, these assignments do not establish the identities or integration status of the other visible signals within the specified retention-time intervals.

Further examination of the original GC-MS data and peak-integration reports is required to determine whether these signals were included in the reported hydrocarbon-class distributions.

File :D:\msdchem\1\data\1405.02.01\Ebrahimzadeh3694AH1.D
Operator : Mousavi
Acquired : 22 Apr 2026 3:00 using AcqMethod QC5.M
Instrument : GC MS
Sample Name: Ebrahimzadeh3630AA.1
Misc Info : Ebrahimzadeh3630AA.1
Vial Number: 15

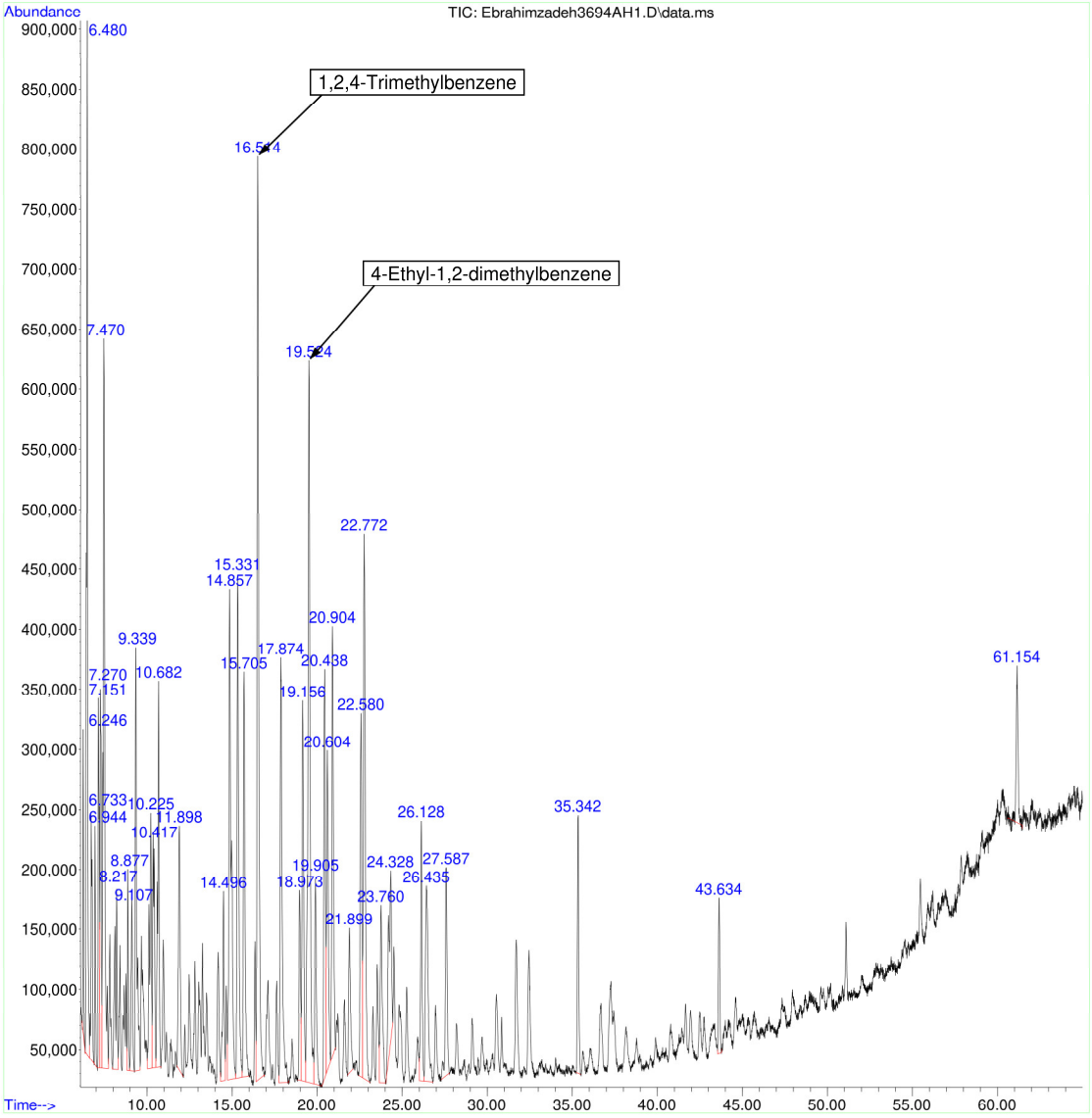


Figure 11. GC–MS total ion chromatogram (TIC) of baseline Al-Daura gasoline (Sample AH1), highlighting the major identified aromatic compounds. The late-eluting signal at 61.15 min remains tentatively assigned. The red baseline segments are automatic peak-integration markers generated by the instrument software.

A late-eluting signal was observed at RT = 61.15 min in the baseline gasoline chromatogram (Figure 11). The original GC-MS library search suggested several octadecenoic acid methyl ester isomers ($C_{19}H_{36}O_2$), including 10-octadecenoic acid methyl ester and methyl oleate. However, these high-boiling compounds are not normally expected as significant constituents of conventional gasoline. Furthermore, because the baseline sample was analyzed before additive treatment, this signal cannot be attributed to the oleic acid precursor used in the synthesis of the hybrid additive. Although the library matches suggest a possible fatty acid methyl ester, the available analytical evidence does not independently

confirm the compound's identity or explain its presence in the baseline gasoline. Possible sample contamination or an uncertain library assignment cannot be excluded. Therefore, the late-eluting signal is considered chemically unconfirmed and is not used to support the proposed additive mechanism or fuel-performance conclusions.

Table 3. Comparison of hydrocarbon-class composition in baseline gasoline and the EDTA@Ni-oleate/ZnO-treated blend based on semi-quantitative GC-MS relative peak areas.

Hydrocarbon Class	Before (%)	After (%)	Δ (Percentage Points)	Interpretation
Isoalkanes (C_8–C_{11})	26.3	21.3	−5.0	Lower relative peak area
n-Alkanes (C_8–C_{16})	8.0	2.6	−5.3	Lower relative peak area
Naphthenes	0.8	0.8	0.0	Minor difference
C_2-aromatics (xylenes)	1.9	2.0	+0.1	Minor difference
C_3-aromatics (TMB, EMB)	24.0	24.0	0.0	Minor difference
C_4-aromatics (TetMB)	31.9	29.1	−2.8	Lower relative peak area
N-containing compounds	1.7	0.0	−1.7	Not reported in treated-sample integration
Prominent peak near 27.59 min	NQ	20.2	—	More prominent in treated chromatogram
Total aromatics	62.0	55.1	−6.9	Lower relative peak area

Abbreviations: TMB = trimethylbenzene; EMB = ethylmethylbenzene; TetMB = tetramethylbenzene; NQ = not reliably quantified; — = not calculated. Δ values were calculated from the original unrounded percentages.

Comparison of the GC-MS total ion chromatograms of baseline gasoline (Sample AH1, Figure 11) and the treated blend (Sample AH2, Figure 12) reveals several corresponding peaks at similar retention times. The most noticeable difference is a prominent signal at RT = 27.589 min in the treated blend, representing 20.22% of its reported relative peak area. A signal was also observed near this retention time in the baseline chromatogram. The treated-sample peak was tentatively assigned to benzaldehyde diethyl acetal ($C_{11}H_{16}O_2$) through mass-spectral library matching. However, its chemical identity and origin were not independently confirmed. Because the chromatograms were displayed using different intensity scales and compound-specific quantitative calibration was not performed, direct comparison of the displayed peak heights cannot establish changes in absolute hydrocarbon concentrations. Therefore, the observed differences are interpreted as changes in relative chromatographic composition rather than definitive evidence of selective hydrocarbon removal.

The investigated gasoline formulation contained approximately 10.05 vol% added toluene, calculated from the nominal blending volumes. Comparison of the baseline gasoline (Figure 11) and treated gasoline (Figure 12) chromatograms showed several corresponding peaks at similar retention times, including approximately 7.47, 9.34, 16.51, and 19.52 min. The aromatic peak assignments in Figure 12 are provisional, based on retention-time correspondence with Figure 11, because independent mass-spectral confirmation for the treated sample was not available. However, the available chromatographic records did not permit a reliable compound-specific assignment of the toluene signal. Therefore, the retention time and peak area of toluene could not be independently verified, and possible co-elution with other gasoline constituents remains unresolved. Because toluene was introduced at a relatively high loading, the absence of its confirmed chromatographic identification represents an analytical limitation. Further examination of the original mass spectra and comparison with an appropriate toluene reference standard are required to establish its chromatographic behavior and concentration reliably.

File : D:\msdchem\1\data\1405.02.01\Ebrahimzadeh3694AH2.D
Operator : Mousavi
Acquired : 22 Apr 2026 4:15 using AcqMethod QC5.M
Instrument : GC MS
Sample Name : Ebrahimzadeh3630AA.2
Misc Info : Ebrahimzadeh3630AA.2
Vial Number : 16

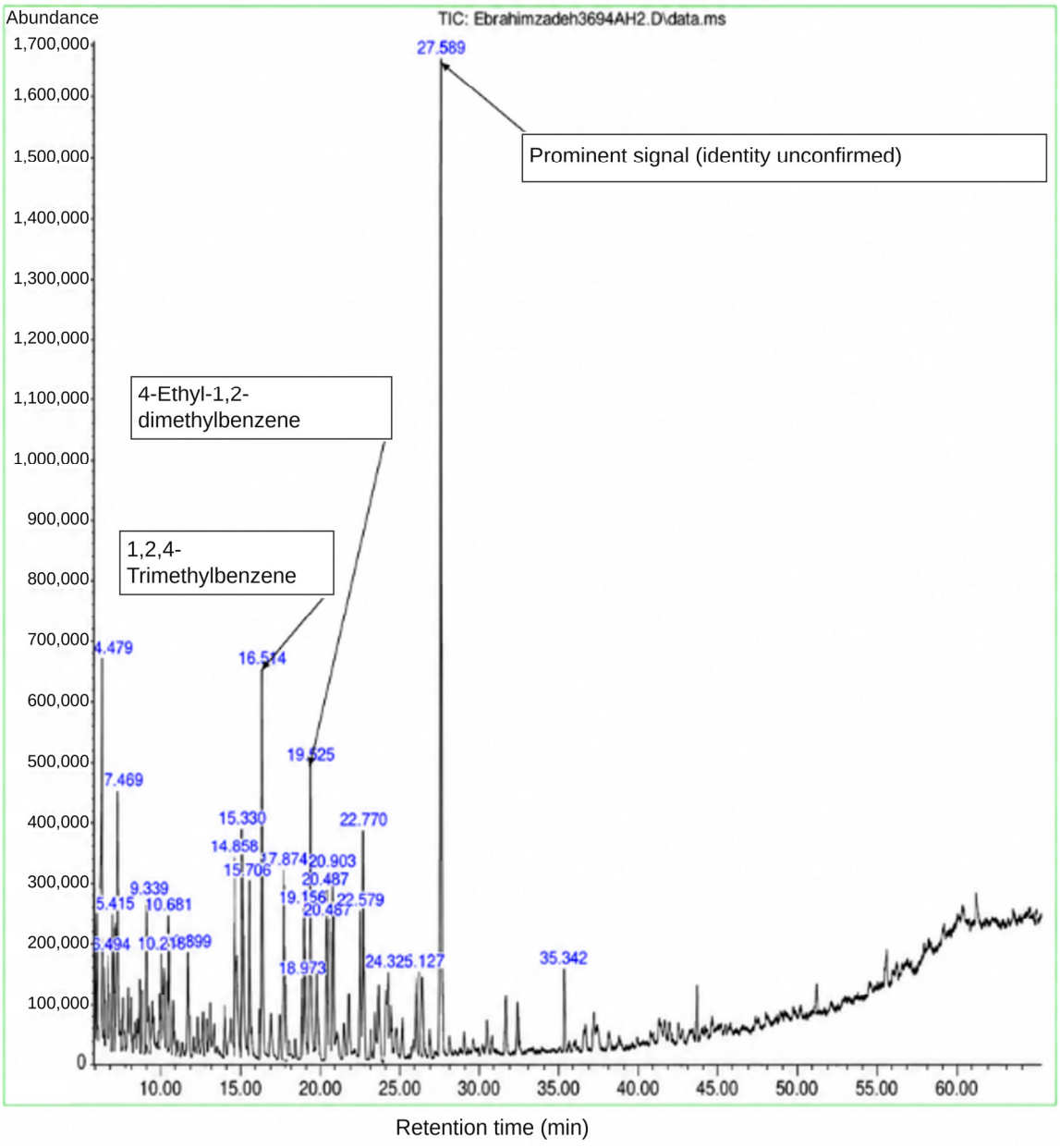


Figure 12. GC–MS total ion chromatogram (TIC) of the EDTA@Ni-oleate/ZnO-treated gasoline blend (Sample AH2), showing the annotated principal aromatic peaks and a prominent signal at RT = 27.589 min with an unconfirmed identity. The peak corresponding to added toluene could not be independently identified from the available chromatographic records.

The summed relative GC-MS peak-area fraction assigned to n-alkanes (C_8–C_{16}) decreased from 7.96% in baseline gasoline to 2.62% in the treated blend, corresponding to a relative decrease of 67.1% based on the reported integration results. However, the available chromatographic records do not provide sufficiently verified compound-specific peak assignments and integrated areas to identify which individual n-alkanes decreased or disappeared. Therefore, selective removal of specific n-alkanes cannot be confirmed. Fur-

thermore, these percentages represent normalized chromatographic peak areas rather than absolute hydrocarbon concentrations. Their values may be influenced by contributions from other detected components, including the prominent signal near 27.59 min, as well as blending dilution and differences in chromatographic response. Consequently, the decrease in the relative n-alkane fraction should not be interpreted as direct evidence of selective adsorption or physical removal. Additional compound-specific quantitative measurements and an appropriate hydrocarbon mass balance would be required to establish actual changes in n-alkane concentrations and their possible contribution to RON enhancement.

The GC-MS results also indicate differences in the relative peak-area fractions assigned to aromatic hydrocarbons in the baseline and treated gasoline samples (Table 3). The C_3-aromatic fraction was approximately 24.0% in both samples, while the C_2-aromatic fraction changed from approximately 1.9% to 2.0%. The C4-aromatic fraction decreased from 31.9% to 29.1%, and the total assigned aromatic fraction decreased from 62.0% to 55.1%. However, these values were obtained from relative GC-MS peak-area integration and should be considered semi-quantitative. Because the treated blend contained additional blending components and the analytical uncertainty of the GC-MS measurements was not determined, the observed differences cannot be interpreted directly as changes in absolute aromatic concentrations. In particular, small differences in individual aromatic fractions should not be regarded as statistically significant without replicate analyses and appropriate quantitative calibration.

The GC-MS results also showed that a nitrogen-containing compound, identified as a hexahydroquinoline derivative, contributed 1.71% of the relative peak area in the baseline gasoline but was not reported among the assigned peaks in the treated-sample integration. This observation may reflect a change in its concentration or relative chromatographic response following treatment. However, the absence of the corresponding peak does not independently confirm complete removal or adsorption by the hybrid additive. Additional quantitative analysis would be required to establish the extent of removal and determine whether interactions with the metal coordination sites contribute to this change.

Molecular basis of RON enhancement: The measured research octane number (RON) increased from 77.0 in the baseline gasoline to 83.5 in the treated blend, corresponding to an overall increase of 6.5 units (Section 2.3.2). The gasoline–toluene reference blend, prepared without the hybrid additive, exhibited a RON of 80.4, demonstrating that toluene contributed substantially to the observed improvement. The additional increase of 3.1 RON units in the complete formulation may be associated with the combined effects of the additive constituents and their interactions with the gasoline matrix. The GC-MS results showed a decrease in the relative n-alkane peak-area fraction from 7.96% to 2.62%, while the relative contributions of several aromatic components changed only slightly. However, these chromatographic changes do not establish selective physical removal of n-alkanes or directly quantify their contribution to RON enhancement. Furthermore, the DFT calculations presented in Section 2.8 investigate the interactions of dibenzothiophene with Ni-EDTA and ZnO models and do not directly evaluate n-alkane adsorption or octane-enhancement mechanisms. Therefore, the observed RON improvement should be attributed to the measured performance of the complete fuel formulation. At the same time, the individual contributions of the hybrid additive constituents and possible hydrocarbon redistribution remain to be established through further controlled experiments.

2.8. Density Functional Theory Computational Analysis: Adsorption Mechanism and Electronic Structure

Density functional theory (DFT) calculations were performed at the B3LYP/LanL2DZ level to investigate possible molecular interactions between dibenzothiophene (DBT) and

simplified ZnO and Ni-EDTA models. Two adsorption complexes were examined: ZnO-DBT and Ni-EDTA-DBT. The calculated frontier molecular orbital parameters and adsorption energies are presented in Table 4, while the HOMO-LUMO energy profile of the Ni-EDTA-DBT complex is illustrated in Figure 13. These calculations provide theoretical insights into the investigated model systems but do not independently validate chemical sulfur adsorption in the experimental gasoline formulation [55–57].

Table 4. Frontier molecular orbital energies and adsorption parameters for ZnO-DBT and Ni-EDTA-DBT complexes were calculated using DFT at the B3LYP/LanL2DZ level of theory.

System	Total E (A.U.)	Eads (kJ/mol)	HOMO (eV)	LUMO (eV)	ΔE (eV)
ZnO + DBT	−612.8793	+388.27	−6.842	−1.215	5.627
Ni-EDTA + DBT	−2113.1369	−841.00	−5.507	−2.430	3.077

Note on aromatic classification: The reported baseline total aromatic-associated peak-area fraction of 61.95% includes the C2-aromatic (1.91%), C3-aromatic (24.00%), and C4-aromatic (31.94%) groups, together with two additional peaks at RT = 26.434 min (2.39%) and RT = 23.759 min (1.71%). The former was tentatively assigned to an ethyltrimethylbenzene isomer, whereas the latter exhibited uncertain aromatic-containing library matches. Consequently, the reported total represents a tentative grouping of aromatic-associated GC-MS signals rather than a fully confirmed aromatic-hydrocarbon concentration. Further mass-spectral verification is required, particularly for the peak at RT = 23.759 min.

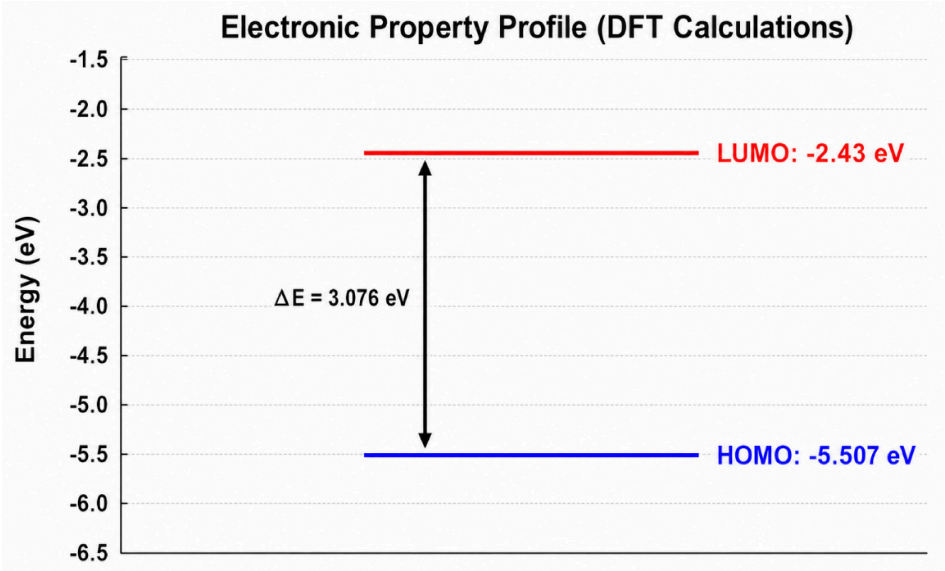


Figure 13. Energy profile of the frontier molecular orbitals for the Ni-EDTA–DBT adsorption complex calculated using the B3LYP/LanL2DZ level of theory in Gaussian 09. HOMO = −5.507 eV; LUMO = −2.430 eV; ΔE = 3.077 eV.

The calculated adsorption energies (Eads) reported in Table 4 differ substantially between the two investigated molecular models. The ZnO-DBT complex exhibited a positive electronic adsorption energy of +388.27 kJ/mol, whereas the Ni-EDTA-DBT complex exhibited a negative value of −841.00 kJ/mol. Under the adopted computational definitions, these results indicate that formation of the optimized Ni-EDTA-DBT model complex is energetically more favorable relative to its isolated components than formation of the investigated ZnO-DBT model complex. However, electronic adsorption energies alone do not establish adsorption spontaneity under experimental conditions because thermal, entropic, solvent, and model-dependent effects were not fully evaluated. Furthermore, the calculated energies require verification against the original computational outputs, particularly regarding molecular charge states, spin multiplicities, and reference energies. Consequently, the

present calculations should not be interpreted as quantitative proof of preferential DBT adsorption or chemical sulfur removal in the investigated gasoline blend.

The calculated highest occupied molecular orbital (HOMO) distribution of the Ni-EDTA-DBT complex is presented in Figure 14. The orbital visualization suggests that electronic contributions may be associated with the nickel coordination environment and the DBT-containing region of the optimized model. The calculated HOMO energy was −5.507 eV. However, the spatial distribution and energy of a single molecular orbital do not independently confirm the formation of a sulfur-to-nickel coordination bond or quantify the strength of such an interaction. Additional analyses, such as charge-density differences, bonding descriptors, or electronic population analysis, would be required to characterize the proposed interaction more conclusively [44,58].

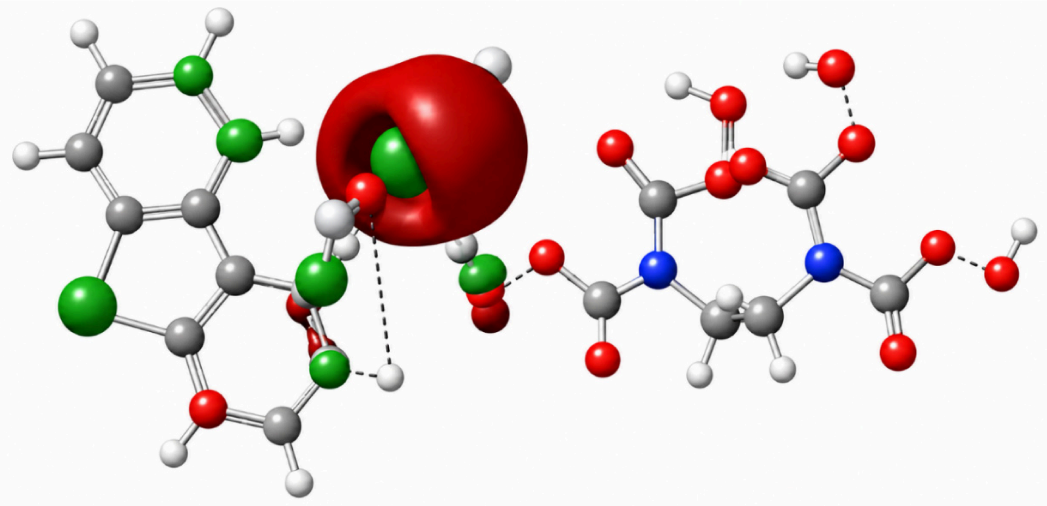


Figure 14. HOMO distribution of the Ni-EDTA-DBT adsorption complex (B3LYP/LanL2DZ). The electron density is concentrated at the Ni coordination center and the sulfur atom of DBT, showing the calculated orbital distribution of the optimized model complex.

The lowest unoccupied molecular orbital (LUMO) of the Ni-EDTA-DBT model complex had a calculated energy of −2.430 eV, as illustrated in Figure 15. The orbital distribution provides information about the electronic structure of the optimized model and the regions that may participate in electron-accepting interactions. However, the LUMO energy and spatial distribution alone do not establish a specific charge-transfer pathway or demonstrate σ-donation and π-back-donation between nickel and DBT. Such interpretations would require additional electronic-structure and bonding analyses [44,58].

The calculated HOMO-LUMO energy gap of the Ni-EDTA-DBT complex was 3.077 eV, compared with 5.627 eV for the ZnO-DBT complex (Table 4), corresponding to an approximately 45.3% smaller gap for the Ni-EDTA-DBT model. This difference indicates distinct electronic structures and may suggest differences in electronic response between the two model complexes. However, a smaller HOMO-LUMO gap does not independently establish faster adsorption kinetics, stronger adsorption, or preferential sulfur removal under experimental conditions [44,58].

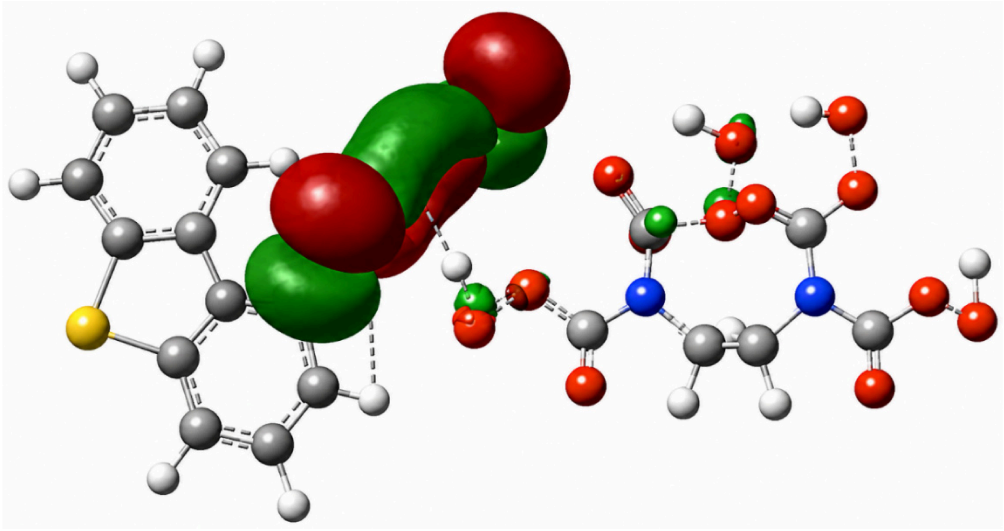


Figure 15. Calculated lowest unoccupied molecular orbital (LUMO) distribution of the optimized Ni-EDTA-DBT model complex at the B3LYP/LanL2DZ level of theory, obtained using Gaussian 09. The calculated LUMO energy is −2.430 eV. The orbital visualization illustrates the electronic distribution of the model complex but does not independently establish a specific charge-transfer pathway or sulfur-nickel bonding mechanism.

Global electronic descriptors were estimated from the calculated frontier orbital energies using Koopmans-type approximations. For the Ni-EDTA-DBT model complex, the estimated ionization potential (IP), electron affinity (EA), chemical hardness (η), chemical softness (S), electronegativity (χ), and electrophilicity index (ω) were 5.507 eV, 2.430 eV, 1.538 eV, 0.325 eV^{-1}, 3.969 eV, and 5.117 eV, respectively. The corresponding ZnO-DBT model exhibited a higher estimated chemical hardness (2.814 eV) and lower electrophilicity index (2.041 eV). These descriptors provide comparative information about the electronic properties of the model complexes. However, they do not independently determine adsorption strength, reaction kinetics, or the chemical nature of the sulfur-metal interaction. The applicability of hard–soft acid–base concepts to the proposed adsorption mechanism therefore remains a qualitative interpretation rather than an experimentally established conclusion.

The DFT calculations indicate differences in the electronic properties and calculated interaction energies of DBT with the investigated Ni-EDTA and ZnO models. These results suggest that coordination-related interactions may be relevant to the proposed sulfur-treatment mechanism. However, the calculations were performed using simplified molecular models that do not reproduce the complete composition or environment of the experimental hybrid additive in gasoline. In addition, the spectroscopic and chromatographic measurements did not independently establish selective sulfur adsorption or complete preservation of aromatic hydrocarbons. Therefore, the proposed metal-sulfur interaction remains a mechanistic hypothesis requiring further experimental and computational verification [46,47].

2.9. Proposed Cooperative Coordination-Adsorption Mechanism

The combined experimental characterization and density functional theory (DFT) calculations provide complementary information about the investigated EDTA@Ni-oleate/ZnO hybrid formulation. FTIR, UV-Vis, DLS, FESEM, and XRD analyses provide information about its physicochemical characteristics, while GC-MS analysis describes changes in the relative chromatographic peak-area distributions of gasoline components. The DFT calculations suggest possible molecular interactions between dibenzothiophene (DBT) and simplified metal-containing models. However, these results do not independently estab-

lish a cooperative adsorption mechanism or confirm the individual contributions of the hybrid components to sulfur reduction, RON enhancement, and RVP control. Therefore, the proposed mechanism should be considered a working hypothesis requiring further experimental validation.

Nanoscale morphology and possible active-site accessibility. The FESEM observations (Section 2.5) reveal morphological features ranging from large aggregates to fine nanoscale structures, while the XRD results (Section 2.6) suggest possible contributions from NiO and ZnO crystalline phases. However, the available data do not independently confirm the chemical composition of individual nanoscale features or establish a specific core–shell architecture. The effective hydrodynamic diameter of 30.5 nm obtained by DLS (Section 2.4) characterizes the freshly prepared dispersion in xylene, as determined using the DLS methodology described in Section 3.3 [50], but does not establish an organic-shell thickness or long-term colloidal stability in gasoline. Although the presence of nanoscale metal-containing domains could influence interactions with sulfur-containing molecules, the density and accessibility of the proposed adsorption sites were not experimentally determined. Additional surface-area, elemental-mapping, and high-resolution structural measurements would be required to evaluate these characteristics.

Possible coordination environment of nickel-containing sites. The FTIR observations discussed in Section 2.1 are consistent with the presence of carboxylate-containing species and possible metal–carboxylate interactions, as described in previous spectroscopic investigations of metal–carboxylate and EDTA-containing complexes [37,40,41]. However, the reported separation between the asymmetric and symmetric carboxylate stretching bands ($\Delta\nu \approx 135\ cm^{-1}$) does not independently establish a unique bidentate coordination geometry or confirm coordinatively unsaturated Ni^{2+} sites. Similarly, the UV-Vis absorption features discussed in Section 2.2 do not conclusively demonstrate ligand-to-metal charge transfer or the availability of Lewis-acid-active nickel centers. EDTA-containing coordination environments may influence the structure and behavior of the hybrid formulation [41,44], but the specific nickel coordination geometry and accessibility of potential sulfur-interaction sites remain uncertain.

Coordination or surface interactions between organosulfur molecules and nickel-containing adsorbents have been investigated as possible pathways for sulfur capture from hydrocarbon fuels [25,28]. Such interactions may also be relevant to the proposed EDTA@Ni-oleate/ZnO formulation, although its specific adsorption mechanism has not been experimentally established. The DFT calculations discussed in Section 2.8 provide model-dependent information about the electronic properties and calculated interactions of dibenzothiophene (DBT) with simplified Ni-EDTA and ZnO models. However, the calculated HOMO-LUMO gaps and orbital distributions do not independently establish the formation of sulfur-nickel bonds or selective adsorption under the experimental gasoline-treatment conditions. Furthermore, the GC-MS results discussed in Section 2.7 do not provide sufficient compound-specific evidence to confirm the selective removal of thiophenic compounds. Therefore, the proposed sulfur-coordination mechanism remains hypothetical. Additional sulfur-speciation measurements, characterization of the separated additive-rich fraction, and a quantitative sulfur mass balance would be required to evaluate the contribution of chemical adsorption to the observed decrease in sulfur concentration.

GC-MS composition and implications for RON enhancement. The GC-MS analysis revealed changes in the relative chromatographic composition of gasoline following treatment with the complete formulation. The summed n-alkane relative peak-area fraction decreased from 7.96% to 2.62%, while the total aromatic relative peak-area fraction changed from 61.95% to 55.06%. However, these changes do not establish selective removal of individual n-alkanes or preservation of aromatic hydrocarbons because the reported values are

normalized chromatographic peak areas rather than absolute concentrations. The original GC-MS library-search report provides tentative identifications of several n-alkanes in the baseline gasoline. However, the corresponding compound-specific changes in the treated blend have not been independently verified. Therefore, the available data do not establish which individual n-alkanes decreased or whether any were selectively removed.

Furthermore, the gasoline–toluene reference blend exhibited a RON of 80.4 compared with 77.0 for baseline gasoline, indicating a substantial contribution from toluene to octane enhancement. The additional increase to 83.5 in the complete formulation may reflect the combined influence of the additive constituents and their interactions with the gasoline matrix. Nevertheless, the available data do not establish a direct relationship between selective n-alkane removal and the measured RON enhancement. Further compound-specific quantitative GC-MS measurements and controlled blending experiments are required to determine the individual contributions of the formulation components [46,47].

The observed changes in chromatographic composition may involve different interactions between the hybrid additive and the hydrocarbon constituents of gasoline. Coordination interactions involving metal centers provide a possible mechanism for the association of sulfur-containing compounds with the additive. In contrast, n-alkanes are nonpolar hydrocarbons without functional groups that would support the proposed Lewis acid–base coordination mechanism. Their possible association with the oleate-containing organic matrix would therefore be expected to involve mainly non-specific dispersion interactions rather than direct coordination to Ni^{2+} sites. However, the present experimental and computational results do not demonstrate preferential adsorption or extraction of n-alkanes. In addition, the relative GC-MS peak-area distributions may be influenced by the introduction of toluene and other additive constituents. Consequently, the apparent decrease in the n-alkane fraction cannot be assigned exclusively to selective removal, and its contribution to the measured RON enhancement remains uncertain.

The regeneration and reuse of the EDTA@Ni-oleate/ZnO hybrid additive were not investigated in the present study. Although sulfur- and nitrogen-containing compounds may interact with the metal coordination sites, the reversibility of these interactions and the possibility of recovering the original additive structure remain unknown. Potential regeneration approaches include solvent washing or chemical desorption after separation of the additive from the treated fuel. However, these methods require experimental validation to determine their effectiveness and effects on additive composition and performance. High-temperature regeneration methods used for conventional solid desulfurization adsorbents may not be directly applicable because the organic Ni-oleate/EDTA matrix could undergo thermal degradation. Therefore, the present formulation should be regarded as a non-regenerated, single-use treatment material under the investigated conditions. Its practical application would require evaluation of additive recovery, residual nickel and zinc concentrations in the treated gasoline, safe handling and disposal of spent material, and overall treatment costs. Further investigations of regeneration efficiency, repeated-use performance, and process economics are necessary before industrial implementation can be considered.

The laboratory-scale treatment involved centrifugation at 3000 rpm for 10 min to separate the sedimented fraction from the treated gasoline before analysis. For potential refinery-scale application, a continuous-flow centrifugal separation system could be considered for recovering the additive-rich fraction from the treated fuel. However, the suitability of this approach for the present colloidal formulation has not been experimentally established. Industrial implementation would require evaluation of separation efficiency, residual nickel and zinc concentrations, equipment capacity, and the possible need for additional fuel polishing. Because gasoline is highly volatile and flammable, appropriate

vapor containment and process safety measures would also be necessary. The recovered material could contain nickel, zinc, residual hydrocarbons, and retained contaminants and would therefore require characterization before selecting suitable metal-recovery, treatment, or disposal methods. Similar waste-management approaches, including de-oiling, metal recovery, and controlled disposal, have been discussed for spent hydroprocessing catalysts by Chen et al. [59]. However, their applicability to the present hybrid additive requires further investigation. From an economic perspective, although ambient-condition operation avoids hydrogen consumption during the blending step, the overall treatment cost would include additive preparation, toluene consumption, separation equipment, utilities, waste management, and possible regeneration. These costs were not quantified in the present study. Therefore, a reliable economic comparison with conventional hydrodesulfurization cannot yet be established. A detailed process design, material balance, and techno-economic assessment are required to evaluate the feasibility of industrial-scale application.

Economic implications of toluene blending: The investigated gasoline formulation contained approximately 10.05 vol% toluene, which represents a substantial blending requirement. The gasoline–toluene reference blend exhibited a RON of 80.4, confirming that toluene contributed significantly to the overall octane enhancement achieved by the complete formulation. Although toluene may be available within refinery aromatic and reformate streams, its use should be evaluated according to its economic value and potential alternative applications. Consequently, the cost of toluene cannot be assumed to be negligible simply because it is produced internally. The total cost of the proposed process would depend on toluene and additive consumption, raw-material prices, additive synthesis, separation equipment, utilities, fuel-quality control, and management of spent material. These costs were not systematically quantified in the present study. Therefore, the economic competitiveness of the proposed formulation relative to conventional gasoline blending or hydrodesulfurization remains uncertain. A detailed techno-economic assessment using refinery-specific material balances, blending-component values, and operating conditions is required before conclusions regarding economic feasibility can be established.

The potential presence of residual nickel- and zinc-containing species in the treated gasoline represents an important safety concern. Although centrifugation was performed before fuel-property measurements, the residual concentrations of nickel and zinc in the clarified gasoline were not determined. Consequently, complete removal of metal-containing particles or dissolved metal species cannot be confirmed. Residual metallic constituents may affect fuel quality, fuel-system components, combustion behavior, and exhaust aftertreatment systems. In particular, nickel tetracarbonyl, $Ni(CO)_4$, is a highly toxic volatile compound that may form through the interaction of metallic nickel with carbon monoxide under suitable conditions. However, its formation in gasoline engines or exhaust systems depends on the chemical state of nickel and the prevailing temperature and gas composition, and was not investigated in the present study. Therefore, quantitative analysis of residual nickel and zinc using validated techniques such as ICP-MS or ICP-OES, together with investigations of nanoparticle separation, combustion emissions, and exhaust aftertreatment compatibility, is essential before the treated fuel can be considered suitable for practical application [60,61].

Ambient-condition operation and comparative advantage: The proposed cooperative mechanism may involve coordination interactions between sulfur-containing compounds and metal-containing sites in the hybrid formulation. However, this mechanism has not been experimentally confirmed. The laboratory blending step was conducted at ambient temperature and pressure without externally supplied hydrogen, elevated temperatures, or pressurized reactors. However, refinery-scale implementation would require additional equipment for additive separation, fuel-quality control, and safe management of the re-

covered material. As a result, the EDTA@Ni-oleate/ZnO system is fundamentally distinct from conventional hydrodesulfurization (HDS; 300–400 °C, 2–6 MPa H_2), oxidative desulfurization (which requires an oxidant and extraction), and extractive desulfurization (which requires a polar solvent and regeneration) [46,47]. Although the proposed treatment operates under ambient blending conditions without hydrogen input, its integration into existing refinery operations would require further assessment of additive separation, residual metal concentrations, spent-material management, and process economics. Therefore, the present findings demonstrate laboratory-scale feasibility rather than established industrial readiness.

Future investigations could also examine the compatibility and performance of the EDTA@Ni-oleate/ZnO hybrid additive in gasoline blends containing renewable oxygenated components, such as ethanol. These studies should evaluate colloidal stability, water tolerance, sulfur concentration, research octane number (RON), Reid vapor pressure (RVP), and possible interactions between ethanol and the hybrid additive. Such experiments are necessary to determine whether the proposed formulation is suitable for gasoline-ethanol blending applications.

3. Materials and Methods

3.1. Materials

Gasoline with a sulfur content of 149.6 ppm, a research octane number (RON) of 77.0, and a Reid vapor pressure (RVP) of 7.9 psi was sourced from the Al-Daura Refinery in Baghdad, Iraq. The sulfur content was measured according to ASTM D5453 using an ANTEK MultiTek ultraviolet fluorescence analyzer (PAC, Houston, TX, USA) [45]. Nickel (II) acetate tetrahydrate (Ni (OAc)2·4H_2O, ≥98%), zinc (II) acetate dihydrate (Zn (OAc)2·2H_2O, ≥99.5%), disodium ethylenediaminetetraacetate (Na2EDTA, ≥99%), oleic acid (≥90%), sodium hydroxide (NaOH, ≥97%), xylene (analytical grade), toluene (analytical grade), and absolute ethanol (≥99.8%) were obtained from commercial suppliers and used without further purification.

3.2. Synthesis of EDTA@Ni-Oleate/ZnO Hybrid Liquid Additive

The hybrid additive was synthesized using a three-step coordination chemistry protocol, as detailed below. Figure 16 schematically summarizes the synthesis route.

Step 1—Synthesis of EDTA@ZnO nanoparticles. Zn $(OAc)_2$·2H_2O (5 g) was dissolved in absolute ethanol (50 mL) under magnetic stirring and heated to 80 °C. Aqueous NaOH solution (2 mL, 1 M) was added dropwise to initiate ZnO nucleation, followed by the addition of Na_2EDTA (1 g) to stabilize the nanoparticles against aggregation [30,31]. The mixture was refluxed at 95 °C for 1 h, yielding a colloidal dispersion designated as EDTA@ZnO for subsequent hybrid preparation. EDTA functionalization of ZnO improves colloidal stability by providing electrosteric repulsion from the polyanionic EDTA corona, which suppresses nanoparticle aggregation in both aqueous and non-aqueous media [30].

Step 2—Synthesis of Ni-Oleate. Ni $(OAc)_2$·4H_2O (10 g) was combined with oleic acid (36 mL) and heated gradually from 110 to 190 °C under atmospheric conditions to promote the formation of nickel oleate through ligand exchange between acetate and oleate species [36]. The reaction mixture was diluted with xylene (36 mL) to reduce viscosity and facilitate handling. The resulting emerald-green Ni-oleate solution was cooled to room temperature and reserved for subsequent use.

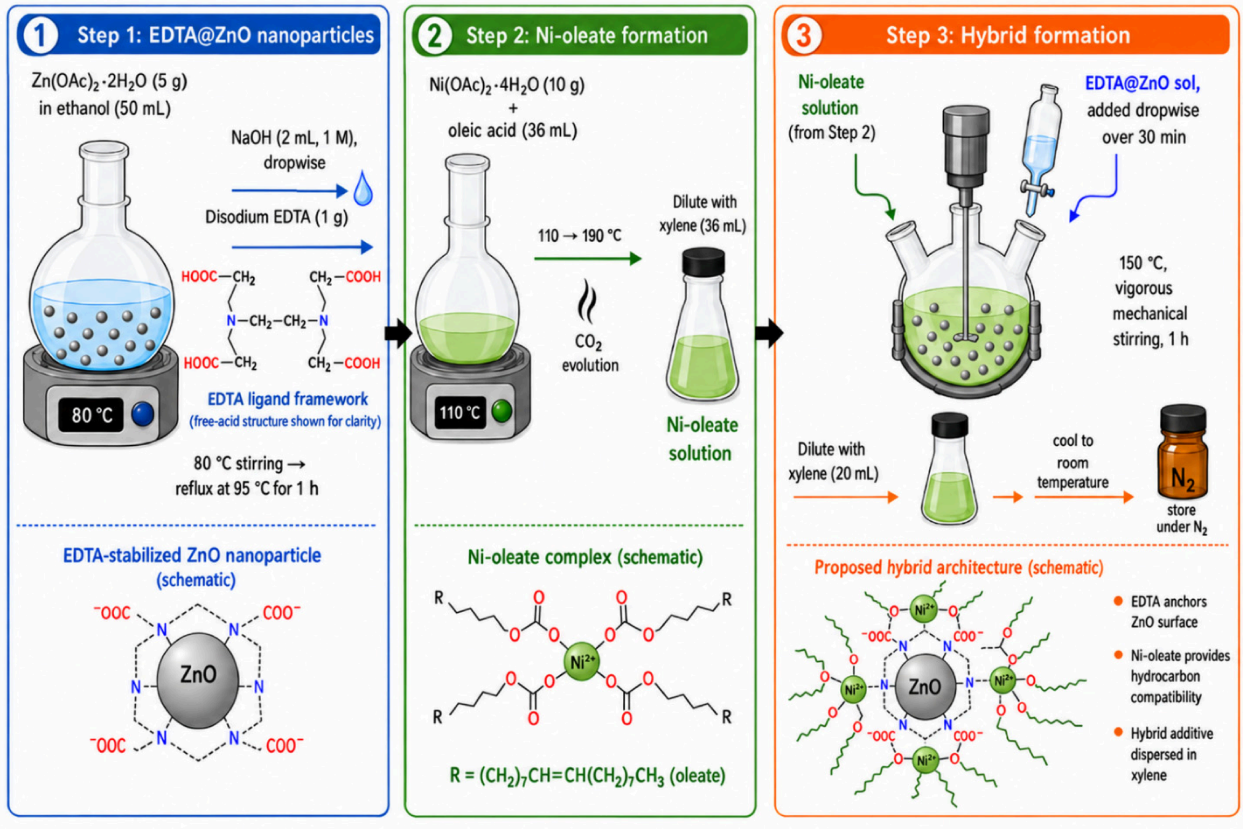


Figure 16. Schematic representation of the three-step synthesis of the EDTA@Ni-oleate/ZnO hybrid liquid additive: (**1**) preparation of EDTA-stabilized ZnO nanoparticles, (**2**) formation of Ni-oleate, and (**3**) formation of the hybrid additive. The molecular structure of EDTA is shown in its free-acid form for clarity, whereas disodium EDTA was used as the experimental reagent. The proposed coordination structures and hybrid architecture are schematic representations rather than experimentally determined molecular arrangements.

Step 3—Hybrid formation. The Ni-oleate solution from Step 2 was reheated to 150 °C under stirring. The EDTA@ZnO sol from Step 1 was added dropwise over 30 min with vigorous mechanical stirring to ensure homogeneous dispersion. The reaction was maintained at 150 °C for 1 h to promote interfacial coordination between the Ni-oleate matrix and the EDTA@ZnO nanoparticle surface [30,36]. The final product was diluted with xylene (20 mL), cooled to room temperature, and stored in sealed amber glass vials under a nitrogen atmosphere to prevent oxidation.

The precursor quantities reported above define the formulation investigated in this study and do not represent an experimentally optimized composition. The impacts of varying the Ni/Zn precursor ratio or the metal-to-ligand proportions were not systematically evaluated. Therefore, the present results do not establish an acceptable composition range or determine how changes in Ni or ZnO loading affect fuel performance and dispersion stability. These influences require a systematic composition study under controlled synthesis and fuel-treatment conditions.

3.3. Physicochemical Characterization

Fourier-transform infrared (FTIR) spectroscopy was performed using a Shimadzu IRTracer-100 spectrometer equipped with an attenuated total reflectance (ATR) accessory. Spectra were acquired over the wavenumber range 400–4000 cm^{-1} at a spectral resolution of 4 cm^{-1}, with 32 co-added scans per measurement. The ATR crystal was cleaned prior to each sample acquisition to ensure background integrity. Spectral analysis focused on

the asymmetric and symmetric COO^- stretching region (1300–1700 cm^{-1}), the metal–oxygen region (400–700 cm^{-1}), and the C-N coordination bands associated with EDTA chelation [36,37].

Ultraviolet–visible (UV-Vis) absorption spectra were obtained using a dual-beam spectrophotometer over the range 195–1100 nm. Matched quartz cuvettes were employed, with analytical-grade xylene in the reference cell to eliminate solvent background. Spectral analysis was conducted to characterize the electronic environment of Ni^{2+} coordination centers, assess ligand-to-metal charge transfer (LMCT) transitions associated with carboxylate-to-Ni^{2+} electron donation, and evaluate the optical absorption properties of the ZnO nanoparticle fraction.

Dynamic light scattering (DLS) measurements were carried out using a Brookhaven Instruments (Holtsville, NY, USA) 90Plus Particle Size Analyzer at a laser wavelength of 659 nm and a fixed scattering angle of 15°. Measurements were performed at a controlled temperature of 25.0 ± 0.1 °C using freshly prepared dispersions in analytical-grade xylene. The reported effective hydrodynamic diameter and polydispersity index (PDI) were obtained from three consecutive measurements of the freshly prepared dispersion, following the measurement principles described in ISO 22412:2017 [50].

Field-emission scanning electron microscopy (FESEM) was conducted using a TESCAN MIRA3 LMU Schottky field-emission SEM (Brno, Czech Republic) operated at an accelerating voltage of 15 kV with secondary electron (SE) detection and a working distance of approximately 10.7 mm. Samples were mounted on aluminum stubs and sputter-coated with a thin gold layer to prevent charge accumulation. Images were collected at magnifications ranging from 54× to 100,000× at two spatially independent sample locations to examine the morphology of the prepared material at different length scales and assess local morphological variations [51].

Powder X-ray diffraction (XRD) analysis was performed on a PANalytical X'Pert PRO diffractometer (Almelo, The Netherlands) using Cu Kα radiation (λ = 1.5406 Å) over a 2θ range of 4.9–80.1° at the Central Laboratory, University of Kashan, Iran. Crystalline phases were identified by comparison with reference patterns from the ICDD PDF-2 database. Mean crystallite sizes were calculated from the principal diffraction peaks using the Scherrer equation ($D = k\lambda/\beta \cos\theta$, $k = 0.89$), with instrumental line broadening corrected using the Caglioti function [62]. The observed diffraction features were compared with reference patterns for ZnO and NiO to assess possible crystalline-phase contributions. Because of peak overlap and the broad background, the phase assignments and crystallite-size estimates were considered tentative.

Gas chromatography–mass spectrometry (GC-MS) analysis of baseline and additive-treated gasoline samples was performed using an Agilent GC-MS system with acquisition method QC5.M at the Central Laboratory, University of Kashan, Iran. Mass-spectral library searches were performed using the NIST08 and W10N14 databases to obtain tentative compound assignments. The available chromatographic records were used to examine differences in the chromatographic profiles and relative peak-area distributions of hydrocarbon groups between the baseline and treated gasoline samples. Because compound-specific quantitative calibration and independently verified identifications were not available, the GC-MS results were interpreted as semi-quantitative rather than absolute hydrocarbon concentrations [63–65].

Chromatographic peak integration was performed using the GC-MS data-processing software (Brookhaven Instruments Corporation, Holtsville, NY, USA). The integration results were used to estimate relative peak-area distributions for the identified hydrocarbon classes. Compound identification was based on mass-spectral library matching, while retention times were used for chromatographic comparison. Peak assignments were

considered tentative when they could not be independently verified. The resulting relative peak-area fractions were treated as semi-quantitative estimates rather than absolute hydrocarbon concentrations.

3.4. Evaluation of Fuel Performance

A representative gasoline blend was prepared by mixing 350 mL of commercial Iraqi unleaded gasoline, 40 mL of analytical-grade toluene, and 8 mL of the EDTA@Ni-oleate/ZnO hybrid additive, corresponding to nominal concentrations of approximately 10.05 vol% toluene and 2.01 vol% hybrid additive in the complete 398 mL formulation. The toluene volume was equivalent to 11.43% of the initial gasoline volume. Toluene was included as an octane-enhancing blending component because the formulation was evaluated for sulfur content, research octane number (RON), and Reid vapor pressure (RVP) together. It was not added as a sulfur-removal reagent. Its contribution to octane enhancement and dilution of the sulfur originally present in the gasoline must therefore be considered when interpreting the performance of the complete blend. The mixture was placed in a sealed glass vessel and mechanically agitated until a homogeneous and visually stable dispersion was achieved. All blending procedures were performed at ambient temperature and pressure. Following blending, the sample was centrifuged at 3000 rpm for 10 min. The clarified supernatant was carefully collected without disturbing the sediment and used for sulfur analysis, RON and RVP measurements, and GC-MS profiling. Toluene was not separately removed and remained a component of the analyzed blend. This procedure separated the sedimented fraction but did not establish complete removal of dissolved additive constituents or particles remaining dispersed in the supernatant. Accordingly, the reported measurements characterize the clarified multicomponent blend after centrifugation. A reference blend containing 350 mL of baseline gasoline and 40 mL of toluene, without the hybrid additive, was also prepared to evaluate the contribution of toluene to octane enhancement. Its RON was measured using ASTM D2699 [66].

The performance of both the baseline gasoline and the additive-treated blend was assessed using internationally recognized standard test methods. Total sulfur content was measured according to ASTM D5453, which utilizes ultraviolet fluorescence detection and is suitable for liquid hydrocarbons with sulfur concentrations ranging from 1.0 to 8000 mg/kg [45]. The research octane number (RON) was determined in accordance with ASTM D2699, using a standardized single-cylinder knock-testing engine under controlled temperature, mixture ratio, and ignition timing conditions. Reid vapor pressure (RVP) was determined according to ASTM D323 at 37.8 °C (100 °F), using the prescribed vapor-to-liquid volume ratio of 4:1.

Sulfur concentration, research octane number (RON), and Reid vapor pressure (RVP) were each measured in triplicate ($n = 3$). The results are reported as mean values with their corresponding standard deviations (SD). The reported standard deviations were 1.8 ppm for sulfur concentration (ASTM D5453), 0.2 RON units (ASTM D2699), and 0.05 psi for RVP (ASTM D323). These values describe the variability of the replicate analytical measurements and do not independently establish the reproducibility of the gasoline blending procedure.

3.5. Computational Methods

Density functional theory (DFT) calculations were conducted using the Gaussian 09 software package (Revision D.01) [55]. The B3LYP hybrid exchange-correlation functional, which combines Becke's three-parameter exchange with the Lee-Yang-Parr correlation functional, was consistently applied [56,57]. The Los Alamos double-zeta effective core potential basis set (LanL2DZ) was used for all atoms, with relativistic effective core potentials (ECPs) for the core electrons of heavy atoms (Ni, Zn) and explicit treatment of valence

electrons [67]. This computational approach is recognized for its efficiency and reliability in modeling transition-metal complexes with Ni^{2+} and Zn^{2+} coordination environments.

The study examined five molecular systems: a ZnO cluster model, a Ni-EDTA coordination complex, dibenzothiophene (DBT) as a model organosulfur compound, and two corresponding adsorption complexes (ZnO-DBT and Ni-EDTA-DBT). Geometry optimizations for all species were performed without symmetry constraints. Harmonic vibrational frequency calculations were then conducted at the same level of theory to confirm that each stationary point represented a true energy minimum on the potential energy surface, as indicated by the absence of imaginary frequencies.

The adsorption energy (E_{ads}) was calculated as follows:

$$E_{ads} = E\ (Complex) - [E\ (Adsorbent) + E(DBT)]$$

where E (Complex) denotes the total electronic energy of the optimized adsorbed system, E (Adsorbent) is the total energy of the isolated adsorbent (ZnO cluster or Ni-EDTA complex), and E(DBT) is the total energy of isolated DBT. All energies were obtained from fully optimized geometries at the B3LYP/LanL2DZ level. A negative adsorption energy indicates that the optimized adsorption complex has a lower calculated electronic energy than the corresponding isolated components at the same computational level. Adsorption energies are reported in both atomic units (Hartree, A.U.) and kJ/mol, using the conversion factor 1 A.U. = 2625.5 kJ/mol.

Frontier molecular orbital (FMO) energies, specifically the highest occupied molecular orbital (HOMO) and lowest unoccupied molecular orbital (LUMO), were obtained from single-point calculations on the optimized geometries and converted from Hartree units to electron volts using the conversion factor 1 A.U. = 27.211 eV. Chemical reactivity descriptors were derived from FMO energies using Koopmans' theorem, where the ionization potential (IP) and electron affinity (EA) are approximated as IP ≈ −EHOMO and EA ≈ −ELUMO, respectively [58]. The HOMO-LUMO energy gap (ΔE = E_LUMO − E_HOMO) was used as a qualitative descriptor of the electronic structure and possible reactivity of the investigated molecular systems. The energy gap alone was not considered sufficient to establish adsorption strength or reaction kinetics. All molecular geometries and frontier orbital surfaces were visualized using GaussView 5.0 [68]. Energy-level diagrams and comparative performance plots were generated using MATLAB R2023b [69].

4. Conclusions

This study investigated the synthesis, physicochemical characterization, and laboratory-scale fuel performance of an EDTA@Ni-oleate/ZnO hybrid liquid additive under ambient gasoline-blending conditions without externally supplied hydrogen. The principal findings are summarized as follows:

1. Spectroscopic characterization: ATR-FTIR analysis revealed characteristic absorption bands associated with aliphatic C-H groups, carboxylate-containing species, and possible metal–oxygen vibrations. The carboxylate stretching-band separation ($\Delta\nu \approx 135\ cm^{-1}$) was consistent with possible metal–carboxylate interactions. UV-Vis spectroscopy provided additional information about the optical properties of the formulation. However, these techniques did not independently confirm a unique nickel coordination geometry, ligand-to-metal charge transfer, or accessible Lewis-acid-active sites.
2. Particle size, morphology, and crystalline structure: DLS measurements of the freshly prepared dispersion in xylene yielded an effective hydrodynamic diameter of 30.5 nm and a PDI of 0.005, indicating a narrow apparent particle-size distribution under the investigated conditions. FESEM revealed morphological features ranging from

large platelet-like fragments to nanoscale aggregates. XRD analysis suggested possible NiO and ZnO crystalline contributions, with preliminary crystallite-size estimates of approximately 17.0 and 21.0 nm, respectively. Nevertheless, the available results did not conclusively establish a specific core–shell architecture, organic-shell thickness, or lamellar bilayer structure.

3. Gasoline performance: The investigated formulation decreased the measured sulfur concentration from 149.6 to 124.0 ppm (17.1%), increased RON from 77.0 to 83.5 (+6.5 units), and reduced RVP from 7.9 to 7.6 psi. The gasoline–toluene reference blend exhibited a RON of 80.4, demonstrating that toluene contributed 3.4 RON units to the overall improvement. The additional 3.1-unit difference observed for the complete formulation could not be attributed exclusively to the nanoparticles. Furthermore, the measured sulfur concentration was 7.6 ppm below the approximate dilution-only estimate of 131.6 ppm; however, this difference did not independently establish chemical sulfur removal because a rigorous mass-based sulfur balance and appropriate component controls were unavailable.
4. GC-MS composition analysis: The relative n-alkane peak-area fraction decreased from 7.96% to 2.62%, corresponding to a relative decrease of 67.1%, while the reported total assigned aromatic fraction changed from 61.95% to 55.06%. These values represent normalized chromatographic peak areas rather than absolute concentrations. Therefore, they do not establish selective n-alkane removal, aromatic preservation, or a direct mechanistic relationship between hydrocarbon composition and the observed RON enhancement.
5. DFT mechanistic insights: DFT calculations at the B3LYP/LanL2DZ level indicated differences in the electronic properties of the investigated Ni-EDTA-DBT and ZnO-DBT models. The calculated HOMO-LUMO gaps were 3.077 and 5.627 eV, respectively. These results provide theoretical insights into possible molecular interactions but do not independently confirm sulfur-nickel bond formation, selective organosulfur adsorption, or the proposed cooperative coordination-adsorption mechanism under experimental gasoline-treatment conditions.
6. Practical limitations and future research: Before considering refinery-scale application, further investigations are required to establish long-term colloidal stability in gasoline, quantitative sulfur removal, additive separation efficiency, residual nickel and zinc concentrations, and the feasibility of additive recovery and regeneration. The approximately 10 vol% toluene loading, potential environmental and fuel-system risks, spent-material management, and overall treatment economics must also be evaluated. Future work should include controlled component-comparison experiments, sulfur and hydrocarbon mass balances, residual-metal measurements, and pilot-scale process assessments to determine whether the observed laboratory-scale performance can be translated into a technically and economically feasible gasoline-treatment process.

Author Contributions: I.A.K.A.-D.: Conceptualization, Writing—Original Draft, Methodology, Computational & Data Curation, Supervision, Project Administration; A.J.S.: Data Curation, Formal Analysis, Writing—Original Draft, Writing—Review and Editing; L.H.M.: Software, Formal Analysis, Visualization; T.A.-J.: Writing—Review and Editing, Validation; B.J.K.: Investigation, Methodology; Z.A.A.O.: Resources, Validation; B.J.K., H.A.S.A., L.S.S., D.A.F., S.T.A.-H. and M.H.A.-D.: Writing—Review and Editing, Validation. All authors have read and agreed to the published version of the manuscript.

Funding: This research received no external funding.

Data Availability Statement: The data supporting the findings of this study are included within the article. Raw instrumental data, including Gaussian 09 output files, GC-MS chromatograms, and XRD raw files, are available from the corresponding author upon reasonable request.

Acknowledgments: The authors express their gratitude to the Central Laboratory of the University of Kashan, Iran, for providing XRD and GC-MS analytical services. Appreciation is also extended to Al-Daura Refinery, Baghdad, Iraq, for supplying the baseline gasoline samples utilized in this study. The authors further acknowledge the support of the College of Chemical Engineering at the University of Technology-Iraq. During the preparation of this manuscript, the authors employed Claude (Anthropic) to enhance readability and language. Following the use of this tool, the authors thoroughly reviewed and edited the content and assume full responsibility for the final published article.

Conflicts of Interest: Authors Ibrahim A. Kareem Al-Dulaimi and Zainab A. Abd Oun were employed by the company MRC (Midland Refineries Company). The remaining authors declare that the research was conducted in the absence of any commercial or financial relationships that could be construed as a potential conflict of interest.

References

1. European Parliament and Council of the European Union. Directive 2009/30/EC of 23 April 2009 amending Directive 98/70/EC as regards the specification of petrol, diesel and gas-oil and introducing a mechanism to monitor and reduce greenhouse gas emissions. *Off. J. Eur. Union* **2009**, *L140*, 88–113. Available online: https://eur-lex.europa.eu/legal-content/EN/TXT/?uri=CELEX:32009L0030 (accessed on 10 November 2026).
2. *GB 18352.6-2016*; Limits and Measurement Methods for Emissions from Light-Duty Vehicles (CHINA 6). Ministry of Ecology and Environment (MEE) & State Administration for Market Regulation (SAMR): Beijing, China, 2020.
3. IMO. *Marine Environment Protection Committee, Resolution MEPC.305(73): Amendments to MARPOL Annex VI, MEPC 73/19/Add.1, Annex 1*; International/IMO: London, UK, 2018.
4. Concawe, Low Carbon Pathways CO_2 Efficiency in the EU Refining System. 2030/2050 Executive Summary (Interim Report), Brussels, 2018. Available online: www.concawe.eu (accessed on 10 November 2026).
5. Hossain, M.N.; Park, H.C.; Choi, H.S. A comprehensive review on catalytic oxidative desulfurization of liquid fuel oil. *Catalysts* **2019**, *9*, 229. [CrossRef]
6. Zhao, J.; Zhang, L.; She, N.; Liu, Y.; Chai, Y.; Liu, C. Interaction between Ni and HZSM-5 in aromatization-enhanced reactive adsorption desulfurization catalysts for FCC gasoline upgrading. *Appl. Petrochem. Res.* **2014**, *4*, 359–365. [CrossRef]
7. Rui, J.; Liu, F.; Wang, R.; Lu, Y.; Yang, X.; McPhee, D.J. Adsorptive desulfurization of model gasoline by using different Zn sources exchanged NaY zeolites. *Molecules* **2017**, *22*, 305. [CrossRef]
8. Ju, F.; Liu, C.; Meng, C.; Gao, S.; Ling, H. Reactive Adsorption Desulfurization of Hydrotreated Diesel over a Ni/ZnO–Al_2O_3–SiO_2 Adsorbent. *Energy Fuels* **2015**, *29*, 6057–6067. [CrossRef]
9. Siddiqui, M.A.B.; Ahmed, S.; Aitani, A.M.; Dean, C.F. Sulfur reduction in FCC gasoline using catalyst additives. *Appl. Catal. A Gen.* **2006**, *303*, 116–120. [CrossRef]
10. Boshagh, F.; Rahmani, M.; Rostami, K.; Yousefifar, M. Key Factors Affecting the Development of Oxidative Desulfurization of Liquid Fuels: A Critical Review. *Energy Fuels* **2021**, *36*, 98–132. [CrossRef]
11. Hosseini, A.; Khoshsima, A.; Sabzi, M.; Rostam, A. Toward Application of Ionic Liquids to Desulfurization of Fuels: A Review. *Energy Fuels* **2022**, *36*, 4119–4152. [CrossRef]
12. Qiu, X.; Wang, B.; Wang, R.; Kozhevnikov, I.V. New Adsorption Materials for Deep Desulfurization of Fuel Oil. *Materials* **2024**, *17*, 1803. [CrossRef]
13. Zhou, G.; Chen, S.; Jiang, W.; Li, Q.; Zhou, H.; Gong, X.; Zhang, X. Deep Adsorption Desulfurization of Fluid Catalytic Cracking Light Gasoline on NiO/ZnO-TiO_2 Adsorbents with a High Breakthrough Sulfur Capacity. *ACS Omega* **2022**, *7*, 11068–11074. [CrossRef]
14. Saha, B.; Vedachalam, S.; Dalai, A.K. Review on recent advances in adsorptive desulfurization. *Fuel Process. Technol.* **2021**, *214*, 106685. [CrossRef]
15. Ganiyu, S.A.; Lateef, S.A. Review of adsorptive desulfurization process: Overview of the non-carbonaceous materials, mechanism and synthesis strategies. *Fuel* **2021**, *294*, 120273. [CrossRef]
16. Omar, R.A.; Verma, N. Review of Adsorptive Desulfurization of Liquid Fuels and Regeneration Attempts. *Ind. Eng. Chem. Res.* **2022**, *61*, 8595–8606. [CrossRef]

17. Fan, J.; Khan, H.A.; Wang, T.; Ruiz-Martinez, J.; Saxena, S.; Emwas, A.H.; Samaras, V.G.; Roberts, W.L. Oxidative desulfurization of fuel oil and molecular characterization of the sulfone compound distribution in the different extractants. *Sep. Purif. Technol.* **2023**, *327*, 124902. [CrossRef]
18. Sager, A.; Rahman, S.; Imtiaz, S.A.; Zhang, Y.; Alodhayb, A.; Georghiou, P.E.; Al-Gawati, M. Oxidative and Extractive Desulfurization of Fuel Oils Catalyzed by N-Carboxymethyl Pyridinium Acetate and N-Carboxyethyl Pyridinium Acetate Acidic Ionic Liquids: Experimental and Computational DFT Study. *ACS Omega* **2024**, *9*, 23485–23498. [CrossRef]
19. Tochtermann, J.; Huber, M.; Korth, W.; Albert, J.; Jess, A. Extraction-Coupled Oxidative Desulfurization (ECODS) of n-Tetradecane as Model Oil under Moderate Conditions Using Molecular Oxygen. *Energy Fuels* **2023**, *37*, 9452–9462. [CrossRef]
20. Wang, P.; Wang, R.; Matulis, V.E. Ionic Liquids as Green and Efficient Desulfurization Media Aiming at Clean Fuel. *Int. J. Environ. Res. Public Health* **2024**, *21*, 914. [CrossRef]
21. Castro, P.S.; Zuniga, G.M.; Holmes, W.; Buchireddy, P.R.; Gang, D.D.; Revellame, E.; Zappi, M.; Hernandez, R. Review of the adsorbents/catalysts for the removal of sulfur compounds from natural gas. *Gas Sci. Eng.* **2023**, *115*, 205004. [CrossRef]
22. Fu, R.X.; Zha, Y.P.; Huang, C.F.; Wang, Q.Q.; Xiong, Z.J.; Liu, M.M.; Liu, J. Metal-organic frameworks in adsorption desulfurization: Recent progress, new trends and future perspectives. *Coord. Chem. Rev.* **2026**, *548*, 217185. [CrossRef]
23. Ghadiri, M.; Ghaemi, A.; Shayanmehr, M. A comprehensive review on exploring the potential and behavior of carbon-based adsorbents in the adsorptive desulfurization processes. *Fuel* **2026**, *404*, 136222. [CrossRef]
24. Yang, R.T.; Hernández-Maldonado, A.J.; Yang, F.H. Desulfurization of transportation fuels with zeolites under ambient conditions. *Science (1979)* **2003**, *301*, 79–81. [CrossRef]
25. Ma, X.; Sprague, M.; Song, C. Deep Desulfurization of Gasoline by Selective Adsorption over Nickel-Based Adsorbent for Fuel Cell Applications. *Ind. Eng. Chem. Res.* **2005**, *44*, 5768–5775. [CrossRef]
26. Shihab, M.A.; Hassan, K.T.; Humadi, J.I.; Saud, A.N.; Madkhali, N.; Alzahrani, S.S.; Šiller, L. High-efficiency oxidative-adsorptive desulfurization of diesel fuel using a hydrophobic cellulose-silica hybrid aerogel. *Fuel* **2026**, *407*, 137565. [CrossRef]
27. Olawuni, O.A.; Sadare, O.O.; Roopchund, R.; Moothi, K. Desulphurisation of synthetic gasoline using nanocellulose crystals derived from waste biomass: Adsorption performance, isotherms, kinetics, and thermodynamics. *Int. J. Environ. Sci. Technol.* **2025**, *22*, 13585–13604. [CrossRef]
28. Ju, F.; Wang, M.; Wu, T.; Ling, H. The Role of NiO in Reactive Adsorption Desulfurization Over NiO/ZnO-Al_2O_3-SiO_2 Adsorbent. *Catalysts* **2019**, *9*, 79. [CrossRef]
29. Poland, R. Oil Soluble Hydrogen Sulfide Scavenge. U.S. Patent US9353026B2, 31 May 2016. [CrossRef]
30. Barrak, H.; Saied, T.; Chevallier, P.; Laroche, G.; M'nif, A.; Hamzaoui, A.H.; Barrak, H.; Saied, T.; Chevallier, P.; Laroche, G.; et al. Synthesis, characterization, and functionalization of ZnO nanoparticles by N-(trimethoxysilylpropyl) ethylenediamine triacetic acid (TMSEDTA): Investigation of the interactions between Phloroglucinol and ZnO@TMSEDTA. *Arab. J. Chem.* **2019**, *12*, 4340–4347. [CrossRef]
31. Gong, T.; Tang, Y. Preparation of multifunctional nanocomposites Fe_3O_4@SiO_2–EDTA and its adsorption of heavy metal ions in water solution. *Water Sci. Technol.* **2020**, *81*, 170–177. [CrossRef]
32. Küçükosman, R.; Yontar, A.A.; Ocakoglu, K. Nanoparticle additive fuels: Atomization, combustion and fuel characteristics. *J. Anal. Appl. Pyrolysis* **2022**, *165*, 105575. [CrossRef]
33. Storozhenko, V.N.; Kamyshnikova, A.S.; Pashchenko, K.P.; Okhlobystin, A.O.; Eremenko, I.L.; Berberova, N.T. Transition Metal (Zn(II), Co(II), Cu(II), Ni(II)) Complexes for the Removal of Acidic Sulfur Impurities from Hydrocarbon Fuel. *Russ. J. Coord. Chem.* **2023**, *49*, S97–S127. [CrossRef]
34. Miar, M.; Shiroudi, A.; Pourshamsian, K.; Oliaey, A.R.; Hatamjafari, F. Theoretical investigations on the HOMO–LUMO gap and global reactivity descriptor studies, natural bond orbital, and nucleus-independent chemical shifts analyses of 3-phenylbenzo[d]thiazole-2(3H)-imine and its para-substituted derivatives: Solvent and substituent effects. *J. Chem. Res.* **2021**, *45*, 147–158. [CrossRef]
35. Zhou, X.; Zhang, L.; Liu, H.; Yang, Q.; Zhu, S.; Wu, H.; Ohno, T.; Zhang, Y.; Wang, T.; Su, D.; et al. The powerful combination of 2D/2D Ni-MOF/carbon nitride for deep desulfurization of thiophene in fuel: Conversion route, DFT calculation, mechanism. *J. Colloid Interface Sci.* **2024**, *658*, 627–638. [CrossRef]
36. Bronstein, L.M.; Huang, X.; Retrum, J.; Schmucker, A.; Pink, M.; Stein, B.D.; Dragnea, B. Influence of Iron Oleate Complex Structure on Iron Oxide Nanoparticle Formation. *Chem. Mater.* **2007**, *19*, 3624–3632. [CrossRef]
37. Justi, M.; de Freitas, M.P.; Silla, J.M.; Nunes, C.A.; Silva, C.A. Molecular structure features and fast identification of chemical properties of metal carboxylate complexes by FTIR and partial least square regression. *J. Mol. Struct.* **2021**, *1237*, 130405. [CrossRef]
38. Younis, K.A.; Mahmood, H.K.; Rahman, K.M.; Hadi, K.S.; Ahmed, S.S. Evaluation of Gasoline Samples from Several Erbil Petrol Stations. *Zanco J. Pure Appl. Sci.* **2023**, *35*, 189–196. [CrossRef]
39. Abdellatief, T.M.M.; Mustafa, A.; Duan, X. Isopropanol as a Renewable Additive in Gasoline Blends: Enhancing Octane Ratings for Sustainable Fuel Solutions. *Renew. Sustain. Energy Technol.* **2025**, *1*, 2. [CrossRef]

40. Lanigan, K.C.; Pidsosny, K. Reflectance FTIR spectroscopic analysis of metal complexation to EDTA and EDDS. *Vib. Spectrosc.* **2007**, *45*, 2–9. [CrossRef]
41. Huang, L.; Zhang, X.; Zhang, Z. Fingerprint characterization of M-EDTA complexes and iron compounds using terahertz time-domain spectroscopy. *J. Mol. Struct.* **2020**, *1204*, 127515. [CrossRef]
42. Khan, M.F.; Ansari, A.H.; Hameedullah, M.; Ahmad, E.; Husain, F.M.; Zia, Q.; Baig, U.; Zaheer, M.R.; Alam, M.M.; Khan, A.M.; et al. Sol-gel synthesis of thorn-like ZnO nanoparticles endorsing mechanical stirring effect and their antimicrobial activities: Potential role as nano-antibiotics. *Sci. Rep.* **2016**, *6*, 27689. [CrossRef]
43. Ramike, M.P.; Ndungu, P.G.; Mamo, M.A. Exploration of the Different Dimensions of Wurtzite ZnO Structure Nanomaterials as Gas Sensors at Room Temperature. *Nanomaterials* **2023**, *13*, 2810. [CrossRef]
44. Housecroft, C.E.; Sharpe, A.G. *Inorganic Chemistry*, 5th ed.; Pearson: Harlow, UK, 2018. Available online: https://www.scribd.com/document/752593041/Housecroft-5th-Edition (accessed on 11 June 2026).
45. *ASTM D5453-19*; Standard Test Method for Determination of Total Sulfur in Light Hydrocarbons, Spark Ignition Engine Fuel, Diesel Engine Fuel, and Engine Oil by Ultraviolet Fluorescence. ASTM International: West Conshohocken, PA, USA, 2019. [CrossRef]
46. Brunet, S.; Mey, D.; Pérot, G.; Bouchy, C.; Diehl, F. On the hydrodesulfurization of FCC gasoline: A review. *Appl. Catal. A Gen.* **2005**, *278*, 143–172. [CrossRef]
47. Stanislaus, A.; Marafi, A.; Rana, M.S. Recent advances in the science and technology of ultra low sulfur diesel (ULSD) production. *Catal. Today* **2010**, *153*, 1–68. [CrossRef]
48. *Standard's ASTM*; D323-20a. ASTM International: West Conshohocken, PA, USA, 2020.
49. Eaton, P.; Quaresma, P.; Soares, C.; Neves, C.; de Almeida, M.P.; Pereira, E.; West, P. A direct comparison of experimental methods to measure dimensions of synthetic nanoparticles. *Ultramicroscopy* **2017**, *182*, 179–190. [CrossRef]
50. *ISO 22412:2017*; Particle size analysis—Dynamic light scattering (DLS). International Organization for Standardization: Geneva, Switzerland, 2017.
51. Goldstein, J.I.; Newbury, D.E.; Michael, J.R.; Ritchie, N.W.M.; Scott, J.H.J.; Joy, D.C. *Scanning Electron Microscopy and X-Ray Microanalysis*, 4th ed.; Springer: New York, NY, USA, 2018. [CrossRef]
52. Langford, J.I.; Wilson, A.J.C. Scherrer after sixty years: A survey and some new results in the determination of crystallite size. *J. Appl. Crystallogr.* **1978**, *11*, 102–113. [CrossRef]
53. Caglioti, G.; Paoletti, A.; Ricci, F.P. Choice of collimators for a crystal spectrometer for neutron diffraction. *Nucl. Instrum.* **1958**, *3*, 223–228. [CrossRef]
54. Speight, J.G. *Handbook of Petroleum Product Analysis: Second Edition*, 2nd ed.; John Wiley & Sons, Inc./Wiley: Hoboken, NJ, USA, 2015. [CrossRef]
55. Frisch, M.J.; Trucks, G.W.; Schlegel, H.B.; Scuseria, G.E.; Robb, M.A.; Cheeseman, J.R.; Scalmani, G.; Barone, V.; Ogliaro, F.; Bearpark, M.; et al. *Gaussian 09, Revision D.01*; Gaussian, Inc.: Wallingford, CT, USA, 2013.
56. Becke, A.D. Density-functional thermochemistry. III. The role of exact exchange. *J. Chem. Phys.* **1993**, *98*, 5648–5652. [CrossRef]
57. Lee, C.; Yang, W.; Parr, R.G. Development of the Colle-Salvetti correlation-energy formula into a functional of the electron density. *Phys. Rev. B* **1988**, *37*, 785. [CrossRef]
58. Koopmans, T. Über die Zuordnung von Wellenfunktionen und Eigenwerten zu den Einzelnen Elektronen Eines Atoms. *Physica* **1934**, *1*, 104–113. [CrossRef]
59. Chen, J.; Sun, S.; Xiao, F.; Tu, G. Advancing total management of oily spent hydroprocessing catalyst: From hazardous waste to circular and eco-sustainable utilization. *J. Environ. Manag.* **2025**, *381*, 125202. [CrossRef]
60. Gidney, J.T.; Twigg, M.V.; Kittelson, D.B. Effect of Organometallic Fuel Additives on Nanoparticle Emissions from a Gasoline Passenger Car. *Environ. Sci. Technol.* **2010**, *44*, 2562–2569. [CrossRef]
61. Yin, F.; Qu, F.; Yang, H.; Wang, F.; Wei, Y.; Sun, S.; Chang, Q.; Zhang, C. The kinetic study of nickel carbonylation to nickel tetracarbonyl: Effect of temperature, pressure and size. *J. Chem. Technol. Biotechnol.* **2025**, *100*, 1838–1847. [CrossRef]
62. Cullity, B.D.; Stock, S.R. *Elements of X-Ray Diffraction*, 3rd ed.; Prentice Hall: Upper Saddle River, NJ, USA, 2001.
63. Stein, S. Mass Spectral Reference Libraries: An Ever-Expanding Resource for Chemical Identification. *Anal. Chem.* **2012**, *84*, 7274–7282. [CrossRef]
64. Wallace, W.E.; Moorthy, A.S. NIST Mass Spectrometry Data Center standard reference libraries and software tools: Application to seized drug analysis. *J. Forensic Sci.* **2023**, *68*, 1484–1493. [CrossRef]
65. Wang, Z.; Fingas, M.; Li, K. Fractionation of a Light Crude Oil and Identification and Quantitation of Aliphatic, Aromatic, and Biomarker Compounds by GC-FID and GC-MS, Part II. *J. Chromatogr. Sci.* **1994**, *32*, 367–382. [CrossRef]
66. *Standard's ASTM D2699-23*; Standard Test Method for Research Octane Number of Spark-Ignition Engine Fuel. ASTM International: West Conshohocken, PA, USA, 2023.
67. Hay, P.J.; Wadt, W.R. Ab initio effective core potentials for molecular calculations. Potentials for the transition metal atoms Sc to Hg. *J. Chem. Phys.* **1985**, *82*, 270–283. [CrossRef]

68. Dennington, R.; Keith, T.; Millam, J. *GaussView*; Semichem Inc.: Shawnee Mission, KS, USA, 2009.
69. The MathWorks Inc. *MATLAB R2023b*; The MathWorks Inc.: Natick, MA, USA, 2023.

Disclaimer/Publisher's Note: The statements, opinions and data contained in all publications are solely those of the individual author(s) and contributor(s) and not of MDPI and/or the editor(s). MDPI and/or the editor(s) disclaim responsibility for any injury to people or property resulting from any ideas, methods, instructions or products referred to in the content.